

**UNCLASSIFIED**  
**432241**  
**AD** \_\_\_\_\_

**DEFENSE DOCUMENTATION CENTER**

**FOR**

**SCIENTIFIC AND TECHNICAL INFORMATION**

**CAMERON STATION, ALEXANDRIA, VIRGINIA**



**UNCLASSIFIED**

NOTICE: When government or other drawings, specifications or other data are used for any purpose other than in connection with a definitely related government procurement operation, the U. S. Government thereby incurs no responsibility, nor any obligation whatsoever; and the fact that the Government may have formulated, furnished, or in any way supplied the said drawings, specifications, or other data is not to be regarded by implication or otherwise as in any manner licensing the holder or any other person or corporation, or conveying any rights or permission to manufacture, use or sell any patented invention that may in any way be related thereto.

432241

DDC FILE COPY

432241

AN EXPERIMENTAL STUDY OF HYPERSONIC LOW-DENSITY  
VISCOUS EFFECTS ON A SHARP FLAT PLATE<sup>2</sup>

by

R. J. Vidal,<sup>1</sup> T. C. Golian,<sup>2</sup> and J. A. Bartz<sup>3</sup>

## ABSTRACT

Heat transfer and pressure data<sup>here</sup> obtained with sharp flat plate models at zero and large angles of attack in the CAL hypersonic shock tunnel are presented. These high Mach number data (Mach 14 to 24) extend from the classical thin boundary layer regime to near-free-molecule conditions and are discussed within the framework of existing theory. The large angle-of-attack results verify viscous shock-layer theory and define the low-density conditions where transport effects at the shock wave (~~shock-wave~~ slip) first become important.

The data obtained at zero angle of attack are compared with theory to define the fluid mechanism that governs the low-density effects. The strong shock-wave approximations, the vorticity interaction, and the shock-wave heating effect are ~~shown to be~~ unimportant in this case. ~~It is shown that~~ for the present experiments the effects of transport processes at the shock wave are numerically small in comparison with surface slip for the sharp flat plate at zero angle of attack, and it is

\* Sponsored by the U. S. Air Force Office of Scientific Research (Contract No. AF49(638)-952).

<sup>1</sup> Principal Engineer

<sup>2</sup> Research Engineer

<sup>3</sup> Associate Engineer

MAR 19 1964

BEST AVAILABLE COPY

postulated that surface slip is the dominant low-density effect.

The slip boundary conditions are discussed to demonstrate that there is a pressure jump at the surface, analogous to the classical velocity and temperature jump. This effect is evaluated using existing theories and is in qualitative agreement with the experimental data. The slip boundary conditions are examined in light of the present experiments at zero angle of attack, and it is shown that the usual first-order boundary conditions are inapplicable for the case of a cold wall,

$$\left( \frac{T_w}{T_o} \approx 0.1 \right).$$

# NOMENCLATURE

$A, B$	Constants determined by the Prandtl number (Eq. (1) )
$b$	Free constant in the velocity jump and enthalpy jump
$C$	Chapman-Rubesin constant
$C_*$	Modified Chapman-Rubesin constant, $\frac{\mu(T_*)}{\mu_\infty} \frac{T_\infty}{T_*}$
$C_p$	Specific heat at constant pressure
$C_H$	Stanton number
$H$	Enthalpy
$k$	Thermal conductivity
$K, M'$	Eq. (30)
$M$	Mach number
$P$	Pressure
$P_0$	Reservoir pressure
$P_0'$	Pitot pressure
$P_r$	Prandtl number
$q$	Rate of heat transfer per unit area
$R$	Gas constant, $\frac{P}{\rho T}$
$Re$	Reynolds number, $\frac{\rho_\infty U_\infty x}{\mu_\infty}$
$T$	Temperature
$T_*$	Modified reference temperature (Eq. (5) )
$u, U$	Velocity
$\bar{u}$	Mean molecular velocity
$x$	Distance measured from plate leading edge
$y$	Distance measured normal from plate surface
$\alpha$	Angle of attack

$\beta$	Eq. (3)
$\gamma$	Ratio of specific heats
$\Gamma$	Eq. (46)
$\delta_0^*$	Boundary-layer displacement thickness without surface slip
$\delta_1^*$	Perturbation boundary-layer displacement thickness due to slip
$\epsilon$	Density ratio across a shock wave
$\lambda$	Molecular mean-free-path
$\mu$	Viscosity
$\rho$	Density
$\phi$	Shock wave angle measured from surface
$\bar{\chi}$	$M^3 \sqrt{\frac{C_*}{Re_x}}$
$\bar{\chi}_e$	Eq. (5)
$\omega$	Eq. (27)
$\Phi, \Theta, \eta, \zeta$	Eq. (12)

#### Subscripts

e	Equilibrium nozzle expansion
n	Nonequilibrium nozzle expansion
o	Reservoir conditions
l	Conditions at the base of the continuum boundary layer
w	Conditions at the wall
$\infty$	Conditions in the free stream
s	Conditions behind shock

## I. INTRODUCTION

The recent interest in manned re-entry vehicles has precipitated a concerted attempt to describe the transition between continuum fluid dynamics and free-molecule mechanics. The problem arises from the need during manned re-entry to maintain the deceleration forces tolerably small while the high kinetic energy associated with orbital or space flight is dissipated in the atmosphere. This dictates that much of the atmospheric flight take place at high altitudes where the ambient density is low, in a transitional regime that falls between classical continuum flows and free-molecule flows.

One aspect of this transitional flow regime is its complexity. If one adopts either the continuum or the kinetic viewpoint, it is necessary to consider a variety of phenomena introduced or influenced by the details of the configuration. The sharp flat plate, which is employed in the present research, is an ideal research tool because the governing low-density phenomena can be isolated and studied with relative ease. Competing low-density effects introduced by the configuration details (for example, shock-wave curvature effects due to nose bluntness) are suppressed with a flat plate.

The problem of a sharp flat plate in low-density supersonic flow has been considered over the past decade. The earliest theoretical work was that of Shen,<sup>1, 2</sup> followed by Lees and Probst, <sup>3</sup> Lees,<sup>4</sup> Li and Nagamatsu,<sup>5</sup> Stewartson,<sup>6</sup> Kuo,<sup>7</sup> and Cheng.<sup>8, 9</sup> The problem has been experimentally investigated at low Mach numbers by Schaaf, et al<sup>10</sup> and by Bertram,<sup>11</sup> and high Mach number investigations have been made by Hammitt and Bogdonoff<sup>12</sup> and by Hall and Golian.<sup>9, 13</sup> As a result of these and other investigations, the viscous interaction problem on a flat plate is well understood in both the weak

and the strong interaction regimes as long as the Mach number and Reynolds number are large enough to suppress the low-density effects neglected in the viscous interaction regimes.

These additional low-density effects cause substantial departures from the thin boundary layer results as the density is decreased. The departures have been qualitatively anticipated on the grounds that as the leading edge is approached, the free-molecule limit must be obtained. However, there has been uncertainty in defining the fluid mechanisms that would govern the initial departures, in specifying a valid theoretical model for use in describing the flow field, and in determining the magnitude of these departures.

The purpose of this paper is to present experimental heat transfer and pressure data, obtained with sharp flat-plate models in the CAL hypersonic shock tunnels, which extend from the thin boundary layer limit to near-free-molecule conditions. The intent is to demonstrate the magnitude of the low-density departures from thin boundary layer theory, to test the available low-density theories, and to identify the dominant fluid mechanism causing the initial departures from the thin boundary layer regime.

In this connection, the applicable theories are reviewed in Section II to establish a basis for interpreting the experimental results. The classical slip boundary conditions are reviewed there to show that there is a pressure jump at the surface which is larger than the usual slip effect. Sections III and IV describe the experimental apparatus and test conditions, and the experimental results are presented and discussed in Section V. The first-order slip boundary conditions are appraised in Section V to show they are inapplicable for the case of a cold wall.



The results for the flat plate at large angles of attack are discussed first. This class of flows is of particular interest since only one low-density mechanism (the transport processes at the shock wave) is important. Thus it is possible to evaluate the magnitude of this mechanism and to show that it is a small effect at zero angle of attack. The more complicated case of a flat plate at zero angle of attack is discussed next. The indications are that the dominant low-density mechanism in this case is slip at the surface.

## II. STATUS OF THEORIES

There is a large body of theoretical literature dealing with the sharp flat plate in the thin boundary layer regime. A comprehensive review of the problem can be obtained from the literature cited in the Introduction. In addition, a substantial body of literature is developing on low-density phenomena. A general review of the field has been given recently by Sherman.<sup>15</sup> The purpose in this Section is to set out the theoretical developments pertinent to the interpretation of the experimental results. In this connection, the theory for wedge flows will be reviewed first in Sub-Section A, emphasizing Cheng's viscous shock-layer theory.<sup>17</sup> The reason for this choice is that this theory provides a solution which yields the Blasius result at high densities and approaches the free-molecule limit for vanishing Reynolds number.

The theoretical results pertinent to the sharp flat plate at zero angle of attack are reviewed in Sub-Section B, beginning with the thin boundary layer (weak and strong interaction) results. One approach to treating low-density effects is to include additional low-density mechanisms in the thin boundary layer results with a perturbation calculation. Each of these mechanisms is reviewed to provide a basis for evaluating their effect. The mechanisms considered here are 1) breakdown of the strong shock-wave approximations, 2) the vorticity interaction, 3) the shock-wave heating effect, 4) molecular processes at the surface (surface slip), and 5) transport processes at the shock wave (shock-wave slip). It is noted that effects stemming from finite shock-wave thickness should be considered. There is presently no theoretical treatment for the sharp flat plate known to the authors for assessing this effect.

Each of the above mechanisms has been discussed in the literature. The vorticity interaction and shock-wave heating effect arise from the assumption

that the local inviscid flow properties are fixed by the local shock-wave angle. Actually, the flow is processed by a stronger portion of the shock wave near the leading edge, and the local flow is nonuniform with a higher temperature. The effects of transport processes at the shock wave has received recent attention and become important when the shock layer becomes fully viscous. Under these conditions, the classical (uniform flow) Rankine-Hugoniot conditions are inapplicable, and it is necessary to account for the gradients behind the shock wave.

In the discussion of surface slip, some detail is given to deriving the slip boundary conditions using the classical Maxwell model. This is done in order to show that there is a pressure jump at the surface, analogous to the velocity jump. In addition it is noted that the classical temperature jump is inconsistent for hypersonic flows, and that conceptual consistency requires that an energy or enthalpy jump be considered.

Another approach to the leading-edge problem on a sharp flat plate is to postulate a flow model independent of the thin boundary layer models, and to seek a solution which applies at the leading edge and approaches the thin boundary layer solutions in the high-density limit. The theories derived from both the continuum viewpoint and the molecular viewpoint are reviewed in the latter paragraph of Sub-Section B.

#### (A) Large Angle Wedge Flows

The wedge flow problem at high Reynolds numbers is classical and has been treated with the assumption that the rate of boundary layer growth is small in comparison with the wedge angle. In this scheme, the wedge pressure is determined by the wedge angle, and the boundary layer characteristics can be calculated using the Blasius solution based on conditions behind the shock

waves.<sup>16</sup> As the density is decreased, one might anticipate the boundary layer displacement effects would become important for certain wedge angles  $\left( \frac{M^2 \chi^2}{\bar{\chi}_e} \ll 1 \right)$ . These first-order effects of boundary layer displacement have been theoretically investigated by Cheng<sup>8, 9</sup> and experimentally verified by Hall and Golian<sup>9, 13</sup> as a part of a more comprehensive study of the combined effects of boundary layer displacement, nose bluntness, and angle of attack. The results approach the strong interaction result in the limit of vanishing wedge angle, and the wedge result in the limit of high density.

The low-density effects in wedge flows have been extensively investigated in a study by Cheng of the blunt-body problem at low Reynolds number.<sup>17</sup> An important feature in this analysis is that if the wedge angle is sufficiently large, one can suppress the effects of the strong shock-wave approximations and the effects of shock-wave heating and the vorticity interaction. Further, it is shown that the effects of surface slip and those associated with the shock-wave structure are of higher order than those due to transport processes at the shock wave. This class of flows is of considerable importance since it isolates a single fluid dynamic mechanism. By examining these flows in theory and experiment, it is possible to determine the ambient stream conditions where the transport effects become important. The experimental data reported in Section V will serve to verify the theory and to demonstrate the magnitude of the effects of transport processes at the shock wave.

#### (B) Zero Angle of Attack

The sharp flat plate at zero angle of attack in low-density, hypersonic flow has been investigated for over a decade, and theoretical solutions are presently available for treating the boundary layer displacement effects.<sup>4, 9</sup> A comprehensive review of this problem and the theoretical treatments may be

found in these papers as well as in Ref. 14. The approach generally employed is to consider two regimes; one of weak interactions ( $\frac{P}{P_\infty} \approx 0(1)$ ) and one of strong interactions ( $\frac{P}{P_\infty} \gg 1$ ). The subsequent discussion will retain this subdivision, but it should be noted that local similarity applies in both regimes, and that the subdivision is necessary only because of the approximations used to describe the pressure ratio across the shock wave.

Weak Interaction Regime. There are several solutions available for the weak interaction regime. The one used here is that given by Hayes and Probstein.<sup>14</sup> Following this development, the surface pressure is, to the first-order in the viscous interaction parameter,

$$\frac{P}{P_\infty} = 1 + \frac{\gamma(\gamma-1)}{2} \left[ \frac{T_w}{T_0} A(P_r) + 2B(P_r) \right] \bar{\chi} + \dots$$

$$\bar{\chi} = M^3 \sqrt{\frac{C}{Re_\tau}} \quad (1)$$

where  $C$  is the Chapman-Rubesin constant relating viscosity to temperature. For a Prandtl number of 0.725,  $A = 0.968$ , and  $B = 0.145$ . In calculating the heat transfer, it is found in Ref. 14 that there is no first-order effect due to the self-induced pressure gradient and that, to the first order in  $\bar{\chi}$ , the heat transfer is identical to the zero-pressure gradient result.<sup>16</sup> Similarly, the effect of the induced pressures on the boundary layer is to cause an over-all decrease in the thickness, but there is no first-order effect on the boundary layer slope. Consequently it is concluded that the weak interaction description of the pressure distribution is accurate to the second order in  $\bar{\chi}$ , and that this result is valid for  $\bar{\chi} \lesssim \frac{\gamma(\gamma-1)}{\frac{T_w}{T_0} A(P_r) + 2B(P_r)}$ .

It is interesting to note that the contribution of the second-order term in the pressure is quite small at the theoretical limit of validity of weak interaction

theory; about 15%. Consequently, only the first-order result for the pressure distribution will be used here. In addition, it should be noted that if the Howarth-Dorodnitsyn transformations are applied to the governing boundary layer equations, it can be demonstrated that local flat-plate similarity applies, and that the error associated with neglecting the pressure gradient terms is of order,  $\epsilon = \frac{\gamma-1}{\gamma+1}$ .<sup>9</sup> Hence, the heat transfer rate in the weak interaction regime can be calculated, assuming a Prandtl number of one, using the general relation for heat transfer given by Cheng.<sup>9</sup>

$$M^3 C_H = 0.332 \bar{\chi} \frac{\frac{P}{P_\infty}}{\sqrt{\frac{1}{L} \int_0^L \frac{P}{P_\infty} dx}} \quad (2)$$

$$\text{for } \frac{P}{P_\infty} = 1 + \beta \bar{\chi}$$

$$M^3 C_H = 0.332 \bar{\chi} \left[ \frac{1 + \beta \bar{\chi}}{\sqrt{1 + 2\beta \bar{\chi}}} \right] \quad (3)$$

$$\text{where } \beta = \frac{\gamma(\gamma-1)}{2} \left[ \frac{T_w}{T_o} A(P_r) + 2B(P_r) \right]$$

The relation in Eq. (3) subsequently will be compared with experimental results.

As noted earlier, there are a number of solutions available for the strong interaction regime. The solution used in the present investigation is that given by Cheng.<sup>9</sup> The advantages in this solution are in the fact that it clearly reveals the role of wall temperature in the strong interaction regime and that the solution takes account of the effects of shock-wave curvature on shock-wave strength by using the Busemann formula for the pressure ratio across the shock wave.

The results for the surface pressure and heat transfer are

$$\frac{P}{P_{\infty}} = \frac{\sqrt{3}}{2} \gamma \bar{\chi}_{\epsilon} \quad (4)$$

$$\epsilon (0.664 + 1.73 \frac{T_w}{T_0}) M^3 C_H = 0.219 \sqrt{\gamma} (\bar{\chi}_{\epsilon})^{\frac{3}{2}} \quad (5)$$

where

$$\bar{\chi}_{\epsilon} = \epsilon (0.664 + 1.73 \frac{T_w}{T_0}) M^3 \sqrt{\frac{C_*}{Re_x}}, \quad \epsilon = \frac{\gamma-1}{\gamma+1}$$

$$C_* = \frac{\mu_*}{\mu_{\infty}} \frac{T_{\infty}}{T_*}, \quad \frac{T_*}{T_0} = \frac{T_w}{T_0} + \frac{1}{2} \left(1 - \frac{T_w}{T_0}\right) - \frac{1}{3} \cos^2 \alpha$$

It will be noted that the Chapman-Rubesin constant in Eqs. (4) and (5) is based on a mean temperature different from that normally used. That aspect of the problem has been critically examined,<sup>9, 17</sup> and it was concluded that this definition yielded a better approximation to the average temperature in the boundary layer.

More recently, solutions have been generated for the boundary layer displacement effects using high-speed computers.<sup>18, 19, 20</sup> In Ref. 18, the local similarity concept is applied throughout the weak and strong interaction regimes and the limits of validity are established. The complete tangent-wedge formula (as opposed to the limiting values often applied in weak and strong interaction theory) for the pressure ratio across an oblique shock wave is applied in the inviscid region, and numerical solutions are presented for a variety of cases. The theory has been tested against existing theories and experimental data and found to be in good agreement.<sup>18</sup>

The Strong Shock-Wave Approximations. The accepted practice in strong interaction developments is to assume that the shock wave is strong. A factor

in the lower limit of validity on  $\bar{\chi}$  is in these approximations. Some insight into these limitations can be obtained by writing down the oblique shock-wave relations for the pressure and density ratio across the shock wave, assuming the wave angle,  $\phi$ , is small.

$$\frac{P}{P_{\infty}} = \frac{2\gamma}{\gamma+1} M_{\infty}^2 \phi^2 - \frac{\gamma-1}{\gamma+1} \quad (6)$$

$$\frac{\rho_{\infty}}{\rho} = \frac{\gamma-1}{\gamma+1} + \frac{\frac{2}{\gamma+1}}{M_{\infty}^2 \phi^2} \quad (7)$$

The strong shock approximations and their limits of validity are

$$\frac{P}{P_{\infty}} \approx \frac{2\gamma}{\gamma+1} M_{\infty}^2 \phi^2 \quad \text{for} \quad \frac{P}{P_{\infty}} \gg \frac{\gamma-1}{\gamma+1} \quad (8)$$

$$\frac{\rho_{\infty}}{\rho} \approx \frac{\gamma-1}{\gamma+1} \quad \text{for} \quad \frac{P}{P_{\infty}} \gg \frac{4\gamma}{(\gamma-1)(\gamma+1)} \quad (9)$$

The limits of validity are cast into this form since the pressure is measured in the experiments and consequently provides a convenient method for assessing the strong shock-wave approximations. It can be seen that the strong shock-wave approximation, as applied to the pressure across the shock wave, is readily satisfied even in the weak interaction regime for  $\frac{P}{P_{\infty}} > 1$ . However, this approximation, when applied to the density ratio, introduces a rather severe limitation which suggests that the strong interaction theory should not apply for pressure ratios of less than about 25. This point will be considered further in connection with the experimental results.



The Vorticity Interaction and Shock Heating Effects. One approximation in strong interaction theory is to assume that the pressure and temperature just outside the boundary layer are equal to those quantities just behind the shock wave at the same chordwise station. Actually, the streamline which intercepts the edge of the boundary layer at this station passed through the shock wave at a more forward station, and hence was processed by a stronger portion of the bow wave; the shock-wave heating effect.

Another assumption made is that the velocity is uniform in the inviscid flow between the boundary layer and shock wave. In the physical situation, the shock wave is curved near the leading edge, thereby producing a nonuniform inviscid flow between the boundary layer and the shock wave. This vorticity interaction, first noted by Ferri and Libby,<sup>21</sup> is important in that it alters the boundary condition to be applied at the edge of the boundary layer.

The effects of shock-wave heating and the vorticity interaction in the strong interaction regime have been quantitatively examined by Lees<sup>22</sup> and subsequently refined by Oguchi.<sup>23</sup> In Ref. 22 it is assumed that the pressure distribution is given by strong interaction theory, and the alterations stemming from these higher-order effects are examined with a perturbation calculation. One assumption made is that the changes in the pressure distribution are small in comparison with the strong interaction result. It is demonstrated that the vorticity at the edge of the boundary layer is invariant with chordwise station, while the shock-wave heating effect is governed by the parameter,  $(M \sqrt{\frac{C}{Re_x}})^{1-\frac{2}{38}}$ . The quantitative effects on surface pressure are estimated by considering the changes stemming from the alterations in the boundary conditions at the edge of the boundary layer. It is demonstrated that for an insulated plate, both the vorticity interaction and the shock-wave heating effect are governed by the

parameter  $M\sqrt{\frac{C}{Re_x}}$  and that the effect is to increase the pressure.

$$\frac{P}{P_\infty} \sim \bar{\chi} \left[ 1 + F(\gamma) \left( M\sqrt{\frac{C}{Re_x}} \right)^{1 - \frac{2}{3\gamma}} + \dots \right]$$

The important point to be noted here is the form of the result. That is, within the framework of this perturbation scheme, the influence of the vorticity interaction and the shock-wave heating can be examined by separating the strong interaction effects and considering  $\frac{1}{\bar{\chi}} \frac{P}{P_\infty}$  as influenced by the parameter,  $M\sqrt{\frac{C}{Re_x}}$ .

Transport Processes at the Shock Wave. One effect which could account for the low-density departures from strong interaction theory is the effect of the transport processes neglected in the strong interaction theoretical model. This mechanism was originally examined by Sedov,<sup>24</sup> was subsequently investigated by Probstein and Kemp<sup>25</sup> and by Cheng<sup>17</sup> in connection with blunt-body flows and has recently been included in a formulation of the sharp flat-plate problem by Probstein and Pan.<sup>26</sup> The problem arises in writing down the classical Rankine-Hugoniot equations for the shock wave, which apply if the shock layer is inviscid. If the shock layer is fully viscous, the classical relations do not apply.<sup>14, 17</sup> However, the Rankine-Hugoniot equations can be generalized for a viscous shock layer to obtain the boundary conditions to be satisfied at the shock wave. These can be cast into the following form ( $Pr = 1$ ) analogous to the surface slip boundary conditions.

$$1 - \frac{u_s}{U_\infty} \approx \frac{2}{\sqrt{\pi(\gamma-1)}} \frac{\lambda_s}{U_\infty} \left( \frac{\partial u}{\partial y} \right)_s \quad (10)$$

$$1 - \frac{H_s}{H_\infty} \approx \frac{2}{\sqrt{\pi(\gamma-1)}} \frac{\lambda_s}{H_\infty} \left( \frac{\partial H}{\partial y} \right)_s \quad (11)$$

where the subscript, **S** , refers to conditions behind the shock wave. Using the following transformation,

$$\Phi_\eta = \frac{u}{U_\infty}, \quad \Theta = \frac{H - H_w}{H_\infty - H_w}, \quad \eta = \sqrt{\frac{Re_L}{\xi}} \int_0^\eta \frac{\rho}{\rho_w} dy, \quad \xi = \int_0^\xi \frac{C_x}{L} \frac{P}{P_\infty} dx$$

and introducing the strong interaction result for the pressure (Eq. (4)., the boundary conditions at the shock wave ( $Pr = 1$ ) are

$$1 - \Phi_{\eta_s} \approx 0.63 M \sqrt{\frac{C_x}{Re_L}} \Phi_{\eta\eta_s} \quad (12)$$

$$1 - \Theta_s \approx 0.63 M \sqrt{\frac{C_x}{Re_L}} \Theta_{\eta_s} \quad (13)$$

It can be seen that under these conditions, the parameter governing the transport processes at the shock wave is  $M \sqrt{\frac{C_x}{Re_L}}$ .

Velocity Jump at the Wall. Slip at the surface is encountered as the density at the wall is decreased until the molecular mean-free-path at the wall becomes appreciable. In this case, one must take account of the molecular energy and momentum exchange at the wall in applying a continuum boundary layer analysis. That is, the velocity at the base of the boundary layer is non-zero, and the temperature at the base of the boundary layer can be different from the wall temperature.

The classical approach to the velocity jump at the wall, as developed by Maxwell, effectively is to regard the boundary layer as a nonuniform continuum flow except for the layer with a thickness of one mean-free-path at the wall. The molecules at the base of the boundary layer are assumed to have a Maxwellian velocity distribution, and it is assumed that the velocity jump is given by

$$u_1 = b_u \lambda_1 \left( \frac{\partial u}{\partial y} \right)_1 \quad (14)$$

where  $\lambda$  is the mean-free-path,  $b_u$  is a constant determining the magnitude of the velocity jump, and the subscript, 1, refers to conditions at the base of the continuum boundary layer. The constant,  $b_u$ , is determined by introducing the tangential momentum accommodation coefficient,  $f_T$ ,\* and conserving the tangential momentum across the free-molecule layer. The conservation of tangential momentum is expressed as follows:

$$\mu_1 \left( \frac{\partial u}{\partial y} \right)_1 = f_T \left[ \rho_1 u_1 \sqrt{\frac{RT_1}{2\pi}} + \frac{1}{2} \mu_1 \left( \frac{\partial u}{\partial y} \right)_1 \right] \quad (15)$$

The term on the left is the net tangential momentum transported through the boundary layer, the first term on the right is the tangential momentum transfer for a Maxwellian gas, and the second term on the right is the additional tangential momentum flux.<sup>27</sup> Substituting Eq. (14) in (15), the free constant is obtained.

$$b_u = \frac{2 - f_T}{f_T} \quad (16)$$

Enthalpy Jump at the Wall. The classical statement for the temperature jump is obtained with a similar computation which is based on conserving energy across the free-molecule layer. It is important to note that in this computation it is implicitly assumed that the gas is quiescent, and hence the computation does not rigorously apply for the hypersonic case. The appropriate statement

---

\* The tangential accommodation coefficient is defined as  $f_T = \frac{\tau_i - \tau_r}{\tau_i}$  where  $\tau$  is the tangential momentum, and the subscripts i and r refer to the incident and reflected quantities.

is that there is a jump in energy or total enthalpy at the wall which can be calculated in a manner analogous to that for the velocity jump.

$$H_1 = H_w + b_e \lambda_1 \left( \frac{\partial H}{\partial y} \right)_1 \quad (17)$$

Introducing the thermal accommodation coefficient,  $a_e$ \*, the conservation of energy across the free-molecule layer is

$$\frac{k_1}{c_{p1}} \left( \frac{\partial H}{\partial y} \right)_1 = a_e \left\{ \frac{1}{4} \left[ \frac{\mu_1}{\lambda_1} u_1^2 + \frac{\gamma+1}{\gamma} P_r \frac{k_1}{\lambda_1} (T_1 - T_w) \right] + \frac{1}{2} \frac{k_1}{c_{p1}} \left( \frac{\partial H}{\partial y} \right)_1 \right\} \quad (18)$$

where the term on the left is the energy transported through the continuum boundary layer, the first term on the right is energy transferred by a Maxwellian gas, and the second term on the right is the additional energy transported to the Maxwellian gas. Substituting Eq. (17) in Eq. (18), the free constant,  $b_e$ , is

$$b_e = \left( \frac{2-a_e}{a_e} \right) \frac{1}{Pr} \left( \frac{2\gamma}{\gamma+1} \right) - \frac{1}{2} \left( \frac{\gamma-1}{\gamma+1} \right) \frac{u_1^2}{\lambda_1 \left( \frac{\partial H}{\partial y} \right)_1} \quad (19)$$

The first term in the above relation is that obtained in the classical calculation of the temperature jump, and the second term is the velocity correction term. The usual argument for neglecting the second term is that it is of second order in the mean-free-path at the wall. It is important to note that the second term can be neglected regardless of the magnitude of the mean-free-path because of the factor,  $\frac{\gamma-1}{\gamma+1}$ . Consequently, the enthalpy jump is approximately equal to the classical temperature jump and for  $Pr = 1$ ,  $\gamma \rightarrow 1.0$ , the velocity jump and enthalpy jump are equal. The heat transfer to the wall is the

---

\* Defined as  $a_e = \frac{E_t - E_r}{E_t - E_w}$  where  $E$  is the energy, and the subscript,  $w$ , refers to the wall conditions.

term on the left in Eq. (18).

$$q = - \left[ k_1 \left( \frac{\partial T}{\partial y} \right)_1 + \mu_1 u_1 \left( \frac{\partial u}{\partial y} \right)_1 \right] \quad (20)$$

This statement of heat transfer to the wall is comparable with that given by Maslen,<sup>28</sup> taking account of the work due to sliding friction.

Pressure Jump at the Wall. The velocity and enthalpy jumps are the hypersonic equivalents of the classical slip boundary conditions usually cited in the literature.<sup>27</sup> It is important to note, however, that the energy and only one component of the momentum have been conserved in deriving these relations; the normal component of momentum has not been considered. In writing the conservation of normal momentum across the free-molecule layer, it can be shown that there is also a pressure jump at the surface. The surface pressure is<sup>14</sup>

$$P_w = (2 - f_n) P_i + f_n P_r \quad (21)$$

where  $P_i$  is the normal momentum flux per unit area incident on the surface and  $P_r$  is the normal momentum flux per unit area of the molecules re-emitted from the surface, assuming they are emitted diffusely, and  $f_n$  is the normal accommodation coefficient.\* In the spirit of the classical slip model, the incident momentum is simply that of a Maxwellian gas with an additional term to account for momentum transport through the boundary layer, which to the second order in  $\lambda_1$  is

$$P_i = m n_1 \bar{u}_1^2 + \lambda_1 \left( \frac{\partial P}{\partial y} \right)_1 \quad (22)$$

---

\* Defined as  $f_n = \frac{P_i - P_r}{P_i - P_w}$

where  $m$  is the particle mass,  $\bar{u}$  is a mean velocity, and  $n$  is the number of incident molecules per unit volume. The continuity requirement across the free-molecule layer is

$$mn_w \bar{u}_w = m_i n_i \bar{u}_i + 2\lambda_i \frac{\partial}{\partial y} (mn_i \bar{u}_i) \quad (23)$$

Combining Eqs. (21), (22), and (23) and using the relations in Ref. 14 for the Maxwellian mass flux and momentum flux it follows that the wall pressure is

$$\frac{P_w}{P_i} = \left(1 - \frac{f_n}{2}\right) \left[1 + \frac{2\lambda_i}{P_i} \left(\frac{\partial P}{\partial y}\right)_i\right] + \frac{f_n}{2} \sqrt{\frac{T_w}{T_i}} \left[1 - \frac{\lambda_i}{T_i} \left(\frac{\partial T}{\partial y}\right)_i + \frac{2\lambda_i}{P_i} \left(\frac{\partial P}{\partial y}\right)_i\right] \quad (24)$$

Within the framework of thin boundary layer analysis, it is usually assumed that the normal pressure gradient is zero. Equation (24) shows that in this case, there is a pressure jump at the surface resulting from the temperature difference across the free-molecule layer. The importance in the pressure jump is that it is a direct effect. The velocity and enthalpy jump are important in that they alter the boundary layer displacement thickness which in turn alters the induced pressure,  $P_i$ . Because of the pressure jump, the wall pressure is different from the induced pressure in direct proportion to the velocity and enthalpy jumps. Evidently this effect has not been previously incorporated in boundary layer analyses that include surface slip.

In concluding this discussion of the slip boundary conditions, it should be noted that the classical computation reproduced above is conceptually inconsistent and consequently somewhat unsatisfying. In particular, in writing down the energy, mass, and momentum balance, it is first assumed that the gas one mean-free-path from the wall has a Maxwellian velocity distribution, implying that the boundary layer properties are constant over some undefined height. The

fact that the boundary layer is non-Maxwellian is taken into account by adding on additional terms proportional to the continuum gradients. The slip boundary conditions have been derived by Patterson from the molecular viewpoint using a perturbation scheme.<sup>29</sup> That calculation assumes the gas is slightly nonuniform and the results, given to the first order in  $\lambda_1$ , are in close agreement with those cited here.

Surface Slip in the Strong Interaction Regime. The classical temperature and velocity jumps have been applied by a number of investigators in analyses of the laminar boundary layer at low densities. The general approach in these calculations is to determine the changes in the boundary layer displacement thickness due to slip, and the attendant changes in induced pressure, skin friction, and heat transfer. One analysis that bears directly on the present results is a perturbation calculation by Aroesty<sup>30</sup> based upon strong interaction theory. The aim there is to examine the importance of surface slip in the strong interaction regime. The analysis is based on the classical first-order slip boundary conditions in which the slip velocity and temperature jump are evaluated at the wall conditions as opposed to conditions at the base of the boundary layer, i. e.

$$u_1 = b_u \lambda_w \left( \frac{\partial u}{\partial y} \right)_w, \quad T_1 = T_w + b_t \lambda_w \left( \frac{\partial T}{\partial y} \right)_w \quad (25)$$

The analysis does not include the pressure jump. The solution is carried to the point of setting out the momentum equation describing the first-order slip effects, which is then solved approximately for the case of an adiabatic wall. This approximate solution is based on the assumption that the primary effect of slip stems from the change in the boundary conditions. The result obtained for the pressure is



$$\frac{P_1}{P_\infty} = P_0 \left[ 1 + \frac{4}{3} \omega \frac{\delta_1^*}{\delta_0^*} \right] \quad (26)$$

where  $P_0$  is the no-slip strong interaction description of the surface pressure (for example, Eq. (4)),  $\delta_0^*$  is the no-slip boundary layer displacement thickness, and  $\omega \delta_1^*$  is the change in displacement thickness stemming from the slip boundary conditions. The parameter,  $\omega$ , in its general form is

$$\omega = \frac{\lambda_w \rho_w U_\infty}{\sqrt{2} \int_0^\infty \rho_w \mu_w U_\infty dx} \quad (27)$$

where  $\lambda_w$  is the molecular mean-free-path at the wall.

By invoking the strong interaction solution for the pressure, within the context of the perturbation analysis, the governing parameter becomes<sup>\*</sup>

$$\omega = \sqrt{\frac{\pi \gamma}{2}} \sqrt{\frac{\gamma-1}{8}} \sqrt{\frac{T_w}{T_0}} \left( M \sqrt{\frac{C_x}{Re_x}} \right)^{\frac{1}{2}} \quad (28)$$

For an adiabatic wall, it is demonstrated that the effect of slip is to decrease the displacement thickness, and the final result for the pressure is

$$\frac{P_1}{P_\infty} = P_0 \left[ 1 - \frac{1}{4} \sqrt{\pi \gamma (\gamma-1)} \sqrt{\frac{T_w}{T_0}} \left( M \sqrt{\frac{C_x}{Re_x}} \right)^{\frac{1}{2}} \right] \quad (29)$$

The analysis concludes that for a Prandtl number of one, there is no slip effect on the heat transfer coefficient.

Leading-Edge Solutions. A number of investigators have examined the low-density leading-edge problem outside the framework of strong and weak

---

<sup>\*</sup> There appears to be a numerical error in Aroesty's original evaluation of this parameter.

boundary layer interactions. The approach used by Oguchi<sup>31</sup> is to postulate a wedge-like continuum flow model with a viscous flow filling the entire region between the body and the shock wave. A solution, assuming slip effects at the surface to be negligible, showed that a limited region of constant pressure should exist at the leading edge. This problem has been re-examined by the same author<sup>32</sup> using the classical (velocity and temperature jump) first-order slip boundary conditions. The inclusion of the classical slip boundary conditions evidently removes an anomaly in heat transfer that appeared in the earlier treatment, and the heat transfer now appears to approach a maximum value. In addition, the governing parameter that arises in this treatment is  $M\sqrt{\frac{C_x}{Re_x}}$ . Experimentally, this suggests a data correlation with this parameter in the strong interaction regime and beyond.

The leading-edge problem has also been treated with kinetic theory by Charwat<sup>33, 34, 35</sup> seeking a solution which consistently yields the free-molecule limit and defines the initial portions of the transition to the continuum regime. The problem is complicated since within the framework of the molecular approach, it is necessary to define the velocity distribution function for the molecules after each collision. The original analysis<sup>33</sup> introduces certain simplifying assumptions to make the problem tractable. The more critical assumptions are: a) the emission from the wall is equal to the cross-stream mass flux in the free stream and invariant with chordwise location, b) the gas is two-dimensional, and c) only the flux of free-stream molecules and molecules that have experienced one collision is considered. The solution for the surface pressure is

$$\frac{P_w}{P_\infty} = \frac{1}{2} e^{-\frac{K}{M'}} \left\{ \left[ 1 + \frac{1}{2} \left( 1 - \frac{U_c}{U_\infty} \right) \frac{M'^2}{K} \left( \exp \left[ -\frac{K}{M'} \{ e^{-K} - 1 \} \right] - 1 \right) \right] \right\} + \frac{1}{2} M' \frac{U_c}{U_\infty} \quad (30)$$

If one assumes a Maxwellian distribution of velocities,

$$K = \frac{\kappa}{\sqrt{2} \lambda_{\infty} \frac{U_e}{U_{\infty}}} \quad \frac{U_e}{U_{\infty}} \approx 2 \sqrt{\frac{\gamma-1}{\pi \gamma} \frac{T_w}{T_0}} \quad M' = M_{\infty} \sqrt{\frac{\pi \gamma}{8}}$$

The heat transfer has been calculated by the present authors from the original analysis as

$$M' C_H + \frac{3}{2} \left( \frac{U_e}{U_{\infty}} \right)^2 \approx \left\{ \left\{ 1 + \frac{5}{6} \frac{M'}{K} \left( 1 - \frac{U_e}{U_{\infty}} \right)^2 \left[ -1 + \exp \left\{ -\frac{K}{M'} (\bar{e}^{-K} - 1) \right\} \right] \right\} \right\} e^{-\frac{K}{M'}} \quad (31)$$

In a subsequent report,<sup>35</sup> the original solutions were modified and free constants introduced in order to minimize the inaccuracies caused by the necessary approximations. These constants were determined by assuming a normal momentum accommodation coefficient of unity and matching the solution with limited experimental pressure data.<sup>36</sup> This procedure is a useful device for empirically correlating various data. However, a consistent application of the determined constants in a relation to calculate heat transfer leads to the conclusion that the thermal accommodation coefficient must be 0.4.<sup>35</sup> Such a result is contrary to the experimental data cited in Section V.

### III. EXPERIMENTAL APPARATUS

The low-density investigations described here were made in the CAL Six-Foot Hypersonic Shock Tunnel. Certain high-density, low Mach number experiments were made with the flat-plate model in the CAL 48" Hypersonic Shock Tunnel to completely span the transition between the classical thin boundary layer regime and the strong interaction regime. Both of these facilities have been reported in available literature<sup>37, 38</sup> and only those aspects of the facilities that have direct bearing on the present results will be described here.

#### A. The Six-Foot Hypersonic Shock Tunnel

The CAL Six-Foot Shock Tunnel utilizes the tailored-interface principle of operation. Its important features, with regard to the present research, are the wide range of test conditions that can be obtained, the mode of operation, and the uniformity of the flow in the test section.

The Six-Foot Shock Tunnel is designed to produce reservoir pressures of 25-2000 atmospheres and reservoir temperatures of 4000 - 8000°K in uncontaminated air. The tunnel is currently operated at reservoir pressures up to 1300 atm. and at reservoir temperatures of 4000 - 7000°K. The present investigations were made at a nominal reservoir temperature of about 4000°K, and over a pressure range of 25 - 450 atmospheres. The mode of operation selected for the research was to use a heated driver (675°K) consisting of a mixture of two parts of hydrogen and one part of helium. With this mixture, effective interface tailoring was obtained at a shock Mach number of about 6.25, producing a reservoir temperature of about 4000°K. This particular reservoir temperature was selected to provide a test section static temperature high enough to prevent liquefaction and to insure that the thermochemical nonequilibrium effects in the

nozzle expansion would be small. This latter consideration is discussed more fully in the next section.

#### B. Tunnel Calibrations

An important consideration in low-density experiments is that of flow uniformity in the test section. The flows were calibrated in the present investigation at each test condition. The calibrations consisted of measuring the distribution of pitot pressures across the test section, using piezoelectric pressure transducers developed at CAL,<sup>39</sup> and measuring the flow angularity on the tunnel centerline with a pair of flat-plate models.

The pitot pressure calibrations, Fig. 1, demonstrate that at low densities, the wall boundary layer tends to close. The lowest test section density ( $Re \approx 350$  <sup>1</sup>/in.) produced a useable inviscid core of about 6 inches. At the higher reservoir pressures, the flow is acceptably uniform over at least the center 3 feet of the test section, and there is no evidence of the wall boundary layer.

The flow angularity calibration was based on the experimental observation that at low densities, a region of nearly constant heat transfer exists over a considerable portion of a sharp flat plate near the leading edge. A pair of small scale models (Fig. 2) were built to obtain detailed heat transfer information in this region. These were mounted with the instrumented surfaces parallel and facing each other, and tested in a null-type experiment. The angle of attack of the array was varied over a small range to determine the flow angularity; that is, the angle at which both models indicated the same heat transfer rates. The advantage in this technique is that in the approach to free-molecule flow, the heat transfer on a flat plate is remarkably sensitive to angle of attack. Typically, a one degree change in angle of attack produces a 70% change in heat transfer

rate. Consequently, flow angularity is measured with a precision of about  $\pm 0.1^\circ$ .

The heat transfer rate used in these calibrations was an average value in the region where the heat transfer rate was essentially invariant with the chord-wise position. Typical results obtained at the lowest density condition used in this research are presented in Fig. 3. The data in the upper half of the figure are plotted as a function of geometric angle of attack, and indicate a flow angularity of about  $0.1^\circ$ . The self-consistency of these data is demonstrated in the lower half of the figure where the indicated angularity has been applied to the data from both models, and plotted as a function of aerodynamic angle of attack. The fact that the data from both models produce a smooth curve demonstrates that the inferred flow angularity is valid. The measured angularity at the other test conditions was  $0.1 - 0.15^\circ$ ; it is concluded that the effects of flow angularity are comparable with or smaller than the experimental scatter.

#### C. Models and Instrumentation

Two flat-plate models were used in the experimental research. The small-scale model, shown in Fig. 2, was designed to investigate the leading-edge region, and consisted of fourteen thin-film (platinum) thermometers mounted on a Pyrex-brand glass plate. This glass plate was bonded to a steel plate. Typically, these thermometers were  $.02'' \times .25''$  and near the leading edge were spaced about  $.02''$  apart. All fourteen gages were located within about  $1''$  from the leading edge, and under typical test conditions, five gages were within one ambient mean-free-path from the leading edge. The first gage was at the leading edge. The gage lead wires were gold films about 2 microns thick, leading to conventional lead wires at the model extremities. The entire model was

coated with titanium dioxide about 0.1 microns thick to prevent electrical shorting in ionized flows. The operating principles of the thin-film gage as well as the coated gage have been described in the literature,<sup>40, 41, 42</sup> and will not be reviewed here.

The leading edge was flat-faced with a thickness estimated to be less than .005". The wedge angle of the lower surface was 30°. During the experiments at zero angle of attack, it was found that the first gage indicated a heat transfer rate about twice that at the next station. It has been determined that this behavior was due to heat conduction from the blunt leading edge and the lower surface. Under free-molecule conditions, the heat transfer to the blunt leading edge and to the wedge lower surface is respectively sixty times and thirty times greater than that to the upper surface. Heat conduction calculations showed this was sufficient to cause a 100% change in indicated heat transfer to the instrumented surface. Experiments were made with the instrumented surface shielded from the flow to measure the heating from both surfaces. These verified the above calculation. This is the first instance known to the authors where the assumption of one-dimensional heat transfer was not valid. Careful consideration of these effects are necessary when investigating low-density leading-edge phenomena. Those data that were affected by this additional heating are not reported.

The large-scale flat plate consisted of a steel plate with detachable leading and trailing edges. The model instrumentation shown in Fig. 4 included platinum thin-film resistance thermometers and piezoelectric pressure transducers. The primary thermometers and pressure transducers were equidistant from the midspan position. Thermometers at spanwise locations were included to provide a continuous check on finite span effects. Similarly, three

chordwise extensions were used to obtain a quantitative measure of effects associated with the finite chord length. The thermometers were on glass buttons, mounted in removable sleeves to facilitate instrumentation changes. The detachable leading edge was instrumented with thermometers up to 0.3 inches from the leading edge, and with a pressure transducer 0.61 inches from the leading edge. The leading edge was honed to a thickness of the order of  $5 \times 10^{-4}$  inches.

The piezoelectric transducers are those described in Ref. 39. Briefly, they are diaphragm-type transducers driving modified lead-zirconium-titanate crystals. The nominal output is 2 volts/psi, and the transducers have been used in the present research to measure pressures as low as  $2 \times 10^{-4}$  psi. An important consideration in low-density experiments is the lag time associated with pressure orifice size and tube internal volume. This aspect was examined within the framework of both continuum and free-molecule concepts.<sup>43</sup> It was concluded that with an orifice area of  $15 \times 10^{-3}$  in.<sup>2</sup>, an orifice length of  $6 \times 10^{-2}$  in., and an internal volume of  $11 \times 10^{-3}$  in.<sup>3</sup>, the lag time should be about 200 microseconds. In the subsequent experiments it was impossible to quantitatively assess the lag time since it was smaller than the tunnel starting time (about 1 millisecond). However, the pressure data were found to achieve a steady value within 200 - 300 microseconds after the thermometers showed the tunnel had started.

In the interests of aerodynamic cleanliness, the large-scale model was supported by 8 wires 1/16" in diameter and attached at the model extremities. The instrumentation lead wires were let out of the model under surface and hidden in the shadow of the lower surface support wires. The support wires



were connected to the tunnel walls through springs to minimize accelerations that could excite the pressure transducers.

All data were recorded on standard oscilloscopes and high-speed oscillographs. Special instrumentation was constructed at CAL to record the low heat transfer levels measured. In order to eliminate the numerical data reduction procedures to relate the measured surface temperatures to heat transfer rates, analogue circuits have been devised to accomplish the numerical integration during the experiment.<sup>44</sup> However, these are effectively filters and thereby attenuate the electrical signal. Recent modifications were made in the circuit networks to include low-noise amplifying stages which decreased the noise level by about two orders of magnitude.<sup>42</sup> During related research,<sup>48</sup> heat transfer levels as low as  $2 \times 10^{-2}$  Btu/ft<sup>2</sup> sec. (corresponding to  $10^{-2}$  °K temperature change in 1 millisecond) were measured with a signal-to-noise ratio of about 15.

#### IV. AMBIENT TEST SECTION CONDITIONS

The experiments in the 48-inch Hypersonic Shock Tunnel were made at reservoir temperatures of about 3000°K and at reservoir pressures of 50-400 atm. These conditions are sufficiently moderate that in the nozzle expansion, the air can be regarded as in thermo-chemical equilibrium. Consequently, the ambient test section conditions were determined following the equilibrium calculation described below.

As noted earlier, the low density experiments in the Six-Foot Hypersonic Shock Tunnel were made at a reservoir temperature of about 4000°K and with reservoir pressures of 25-450 atm. These conditions were selected to prevent liquefaction in the test section and to minimize the thermochemical nonequilibrium effects in the nozzle expansion. The alterations due to nonequilibrium were taken into account by calculating the test section conditions assuming an equilibrium nozzle expansion, and then introducing the changes stemming from nonequilibrium.

The reservoir conditions for near-tailored-interface operation are determined, using equilibrium air calculations, by measuring the speed of the incident shock wave and the reservoir pressure. The departures from ideal tailored-interface conditions are taken into account by assuming isentropic wave processes caused the observed departures. The equilibrium test section conditions are determined, assuming an isentropic expansion, from the measured pitot pressure and the hypersonic approximations

$$H_0 \approx \frac{1}{2} U_\infty^2 \quad (32)$$

$$P_0' \approx \rho_\infty U_\infty^2 \left(1 - \frac{\epsilon}{2} + \dots\right) \quad (33)$$

where  $\epsilon$  is the density ratio across a normal shock wave and  $P_0'$  is the pitot pressure. The results of this procedure have been checked with exact

numerical results and have been found to be accurate to  $\pm 0.4\%$  over the range of test conditions covered here.

The effects of thermochemical nonequilibrium in the nozzle expansion were calculated using the computer program developed by Eschenroeder, et al.<sup>45</sup> Results obtained with this machine program were recently compared with limited experimental data by Hall, et al.<sup>46</sup> and found to be in good agreement. Equilibrium and nonequilibrium solutions were obtained for reservoir conditions approximating those obtained in the experiments;  $T_0 = 4000^\circ\text{K}$ ,  $P_0 = 25, 100, 300 \text{ atm}$ . These solutions were run only to an axial station in the nozzle expansion where the flow was completely frozen and could be regarded as ideal. The solutions were then extended to the test section conditions by assuming an isentropic expansion and a specific heat ratio  $\gamma = 1.4$ . The important item to be noted in this procedure is that both the equilibrium and nonequilibrium solutions must be extended to the measured pitot pressure.

A discussion of the aerodynamic parameters pertinent to the present research is given in Sections II and V. A tabulation of the nonequilibrium corrections to these parameters is given in Table I for each of the three nominal reservoir conditions used in this research. The subscripts,  $n$  and  $e$ , refer to nonequilibrium and equilibrium values, respectively. The important item to be noted in Table I is the magnitude of the nonequilibrium corrections to certain of the established aerodynamic parameters. For example, consider the strong interaction parameters,  $M^3 C_H$ ,  $\frac{P}{P_\infty}$  and  $\bar{\chi}$ , at a reservoir pressure of 25 atm. The nonequilibrium corrections are respectively 53%, 26%, and 14%. This illustrates that careful attention must be given to nozzle nonequilibrium effects when interpreting conventional aerodynamic test information obtained even at the modest temperature of  $4000^\circ\text{K}$ .

TABLE I

Nozzle Nonequilibrium Effects on the Governing  
Aerodynamic Parameters

$$T_0 = 4000^\circ\text{K}$$

$P_0$	25 atm	100 atm	300 atm
$\frac{H_{0e}}{H_{0n}}$	1.142	1.076	1.026
$\frac{C_{Hn}}{C_{He}}$	1.068	1.037	1.013
$\frac{M_n}{M_e}$	1.123	1.044	1.023
$\frac{Re_n}{Re_e}$	1.543	1.220	1.090
$\frac{(M^3 C_H)_n}{(M^3 C_H)_e}$	1.532	1.183	1.086
$\frac{(P/P_\infty)_n}{(P/P_\infty)_e}$	1.260	1.090	1.046
$\frac{\bar{\chi}_n}{\bar{\chi}_e}$	1.138	1.059	1.036
$\frac{(M^3 C_H / \bar{\chi}^{\frac{3}{2}})_n}{(M^3 C_H / \bar{\chi}^{\frac{3}{2}})_e}$	1.182	1.096	1.033
$\frac{(\frac{1}{\bar{\chi}} P/P_\infty)_n}{(\frac{1}{\bar{\chi}} P/P_\infty)_e}$	1.068	1.037	1.013
$\frac{(M/\sqrt{C^*})_n}{(M/\sqrt{C^*})_e}$	1/1.068	1/1.037	1/1.013

## V. EXPERIMENTAL RESULTS

The experimental program consisted of testing the large-scale and small-scale flat plates at zero-angle of attack and at large angles of attack. Surface pressure and heat transfer rates were measured in all experiments with the large-scale flat plate, but only heat transfer data will be reported for the wedge-flow experiments. The pressure data from those experiments generally confirmed the theoretical conclusion that the surface pressure would be the ideal wedge pressure. The wedge flow experiments will be discussed first to demonstrate the dominant effects due to transport processes at the shock wave.

### A. Wedge Flow Results

As indicated previously, one important aspect of low density wedge flows is that they offer a means for isolating a single fluid dynamic mechanism and studying it in detail. In the theoretical study<sup>17</sup> it was shown that the effects of all other mechanisms were numerically small in comparison with that due to the transport processes. The purpose of the experiments is to verify the theoretical results, duplicating as closely as possible the theoretical assumptions.

One important experimental requirement in checking the theory is on the wedge angle. The competing low density effects can be suppressed and certain of the theoretical assumptions are valid only if the wedge angle is sufficiently large. However, the theory assumes that the shock wave is attached, which requires that the wedge angle be less than about 42°. For these reasons, the verifying experiments were made with wedge angles of 20°, 30°, and 40°. These results are presented and compared with the theory in Fig. 5. It can be seen that the experimental results are generally in good agreement with the theory with the experimental data falling somewhat above the theory. In the high density limit (large values of  $\frac{1}{\cos \alpha} \frac{Re_*}{\gamma M^2 C_*}$ ),

the theory approaches the Blasius solution for  $Pr = 1$ . The average of the experimental data falls some 10%-15% above the Blasius limit, suggesting that the difference between theory and experiment can be attributed to the assumption of  $Pr = 1$ . As a check on this hypothesis, a semi-empirical formula<sup>16</sup> which takes account of Prandtl numbers different from unity was compared with the results in the high density limit. This approximate calculation was about 7% above the theory, lending support to the hypothesis that the observed differences between theory and experiment are due to differences in Prandtl number.

An important consideration in wedge flow experiments is the effect of a finite wedge length. The theory is based upon a semi-infinite model, while experiments must use finite model lengths. The experiment then has a strong expansion fan situated at the model trailing edge which can influence the upstream portion of the model through the subsonic portions of the viscous layer. This effect can be evaluated by comparing the data obtained with the large scale and small scale models at comparable test conditions. Some of the instrumentation on both models were at equivalent chordwise stations. The effects of finite chord length should be negligibly small for the leading edge instrumentation on the large model. If there is a trailing edge effect, it should be apparent in the data from the small scale model. The comparison in Fig. 6 shows the data from the two models agree well in the regions where there was instrumentation duplication and that there is no systematic difference between the data from the two models.

The range of wedge-angles over which the theory is applicable is important. The data reported here show the theory is valid for wedge angles of 20°-40°; experiments are now in progress to better define that range. Preliminary results show that the theory is not applicable for wedge angles of 10°, and is not applicable near

the leading edge for wedge angles that cause shock wave detachment. The experiments indicate the theory does apply over certain portions of the wedge for angles as large as 75°.

Two conclusions from the wedge flow results have bearing on the zero-angle of attack experiments. First, the theory is adequate over the entire density range (from the thin boundary layer regime to the free-molecule limit), although small inaccuracies (10%-15%) apparently stem from the assumption of  $Pr = 1$ . Second, since the dominant fluid mechanism causing the low density departures from the thin boundary layer regime is the transport processes, these results provide a basis for determining the conditions when transport effects first become evident. Comparing the faired curve (averaging the high density data) with the low density data, it can be seen that the low density departures begin at

$$\frac{1}{\cos \alpha} \frac{Re_x}{\gamma M^2 C_x} \approx .3 \text{ to } .4. \text{ In terms of the parameter to be used in examining the zero angle of attack data, this expression conservatively corresponds to } M \sqrt{\frac{C_x}{Re_x}} \approx 1.$$

#### B. Zero-Angle of Attack

The flat plate experiments at zero angle of attack covered a range of Mach numbers and Reynolds numbers to include the transition from the weak to the strong interaction regime through the approach to free-molecule flow. Heat transfer measurements will be reported for Knudsen numbers as large as  $\frac{\lambda_\infty}{\tau} = 5$ , and pressure measurements will be reported for Knudsen numbers as large as 1/5. Since the greatest body of theoretical work is derived from the continuum viewpoint, the data will be discussed with the aim of improving the understanding in this area and explaining the departures from established continuum theory. Separate comparisons will be made with the applicable leading edge solutions.

Transition Between Weak and Strong Interactions. The heat transfer and pressure data obtained at zero angle of attack have been cast into the viscous interaction parameters and are presented in Figs. 7 and 8. The heat transfer data are compared with the theory for zero pressure gradient, the weak interaction theory derived from the first-order result for the pressure (Eq. 3), and with strong interaction theory from Ref. 9 (Eq. 5). Lees' theory<sup>4</sup> is nearly coincident with that shown, and is not included here. The pressure data are compared with the first-order weak and the strong interaction theories, Eqs. (1) and (4), as well as with that of Ref. 4. It can be seen that there are notable departures from strong interaction theory at small and large values of  $\bar{\chi}$ .

The departures exhibited by the heat transfer data at low values of  $\bar{\chi}$  define the transition to the weak interaction regime. This behavior was critically examined in previous experiments.<sup>9, 13</sup> This transition in heat transfer is accurately predicted within weak interaction theory if the higher order terms are retained in the heat transfer formula, Eq. (3). Figure 7 indicates that the transition between the two regimes is rather narrow, and for practical purposes, it is defined by  $5 < \bar{\chi} < 20$ . The correlation of the pressure data with weak and strong interaction theories, Fig. 8, shows larger departures. The data at the smallest values of  $\bar{\chi}$  agree well with both weak and strong interaction theory, indicating the transition regime.

Strong Shock Wave Approximations. It was noted earlier that the strong shock wave approximations evidently could impose severe limitations on strong interaction theory, especially as they influence the density ratio. The inferred limits, given by Eqs. (8) and (9), suggest the theory should break down for  $\frac{P_1}{P_\infty} \lesssim 25$ . The agreement between theory and experiment for  $\frac{P_1}{P_\infty} \approx 2-3$ ,



$\bar{\chi} \approx 10-20$ , especially away from the leading edge (decreasing  $\bar{\chi}$ ), suggest that the strong shock wave approximations do not impose any effective limit on theory. Indeed, the agreement between theory and experiment is as good for  $\frac{P}{P_\infty} \approx 2$  as for  $\frac{P}{P_\infty} \approx 20$ .

The data in Figs. 7 and 8 show large departures from strong interaction theory at large values of  $\bar{\chi}$ . This behavior has been experimentally observed by others.<sup>36, 47</sup> In that work, it was hypothesized that these departures stemmed from the effects of velocity slip and temperature jump at the surface. This conclusion was reached on the basis of correlations similar to those in Figs. 7 and 8 and on the basis of Schlieren observations. In view of the competing low density effects described in Section II that exist in the strong interaction regime, and the importance of identifying the governing mechanisms, a more critical assessment of this hypothesis is warranted.

Low Density Effects on Viscous Interactions. Before proceeding with the discussion of the higher-order fluid dynamic mechanisms, it must be noted that some of the low density departures observed in Figs. 7 and 8 could stem from finite trailing edge effects. To check this possibility, the large scale flat-plate model was tested at one of the lower density conditions with three different trailing edge configurations; the test trailing edge extension (5" long), no trailing edge extension, and a 10" trailing edge extension. Typical results of this investigation are shown in Fig. 9. The form for presenting the data here will be developed subsequently. The important item is the fact that the data with all three trailing edge configurations agree within the scatter of the data, demonstrating that no discernable effect due to a finite trailing edge was present.

It was stated earlier that four effects neglected in the strong interaction regime are the vorticity interaction, the shock wave heating, the effects of surface

slip and the effects of transport processes at the shock wave. Moreover, these four effects are all governed by the same parameter,  $M\sqrt{\frac{C^*}{Re_x}}$ , and because of the perturbation analysis used in the derivations, the effects all enter in the same manner.

$$\frac{P}{P_\infty} \sim \bar{\chi} \left[ 1 + \text{CONST.} \left( M\sqrt{\frac{C^*}{Re_x}} \right)^n \right]$$

$$M^3 C_H \sim \bar{\chi}^{\frac{3}{2}} \left[ 1 + \text{CONST.} \left( M\sqrt{\frac{C^*}{Re_x}} \right)^m \right]$$

The importance of these four effects in the strong interaction regime can then be examined in correlations of  $\frac{1}{\bar{\chi}} \frac{P}{P_\infty}$  vs  $M\sqrt{\frac{C^*}{Re_x}}$  and  $\frac{M^3 C_H}{\bar{\chi}^{\frac{3}{2}}}$  vs  $M\sqrt{\frac{C^*}{Re_x}}$ . These correlations are shown in Figs. 10 and 11 and are compared with strong and weak interaction theories. The equations for each of these theories in terms of  $M\sqrt{\frac{C^*}{Re_x}}$  follow from Eqs. (1), (3), (4), and (5).

Weak Interaction:

$$\frac{1}{\bar{\chi}} \frac{P}{P_\infty} = \beta + \frac{1}{M\sqrt{\frac{C^*}{Re_x}}} \quad (34)$$

$$\frac{M^3 C_H}{\bar{\chi}^{\frac{3}{2}}} = \frac{0.332}{M} \left[ \frac{1 + \beta M^2 \left( M\sqrt{\frac{C^*}{Re_x}} \right)}{\left( M\sqrt{\frac{C^*}{Re_x}} \right)^{\frac{1}{2}} \sqrt{1 + 2\beta M^2 \left( M\sqrt{\frac{C^*}{Re_x}} \right)}} \right] \quad (35)$$

where

$$\beta = \frac{\gamma(\gamma-1)}{2} \left[ \frac{T_w}{T_o} A(P_r) + 2B(P_r) \right]$$

Strong Interaction:

$$\frac{1}{\bar{\chi}} \frac{P}{P_\infty} = \frac{\sqrt{3}}{2} \gamma E \left( 0.664 + 1.73 \frac{T_w}{T_o} \right) \quad (36)$$

$$\frac{M^3 C_H}{\bar{\chi}^{\frac{3}{2}}} = 0.219 \sqrt{\gamma E \left( 0.664 + 1.73 \frac{T_w}{T_o} \right)} \quad (37)$$

Strong interaction theory appears in Figs. 10 and 11 as a horizontal line which varies only with the wall temperature ratio. The departures from the strong interaction regime are then evident as an increase and a decrease in  $\frac{1}{\bar{\chi}} \frac{P}{P_{\infty}}$  and  $\frac{M^3 C_H}{\bar{\chi}^{\frac{3}{2}}}$  at the weak interaction limit and the low density limit, respectively. It should be noted in Eqs. (34) and (35) that this is not a generalized correlation in that there is a Mach number dependence in the weak interaction regime.

Figure 10 shows that the heat transfer data correlate well in both the weak interaction and the strong interaction regimes, and that this correlation is quite satisfactory for defining a low-density limit to the strong interaction regime; that is,  $M \sqrt{\frac{C^*}{Re_x}} \lesssim 1/5$ . The scatter in the weak interaction and strong interaction regimes is about + 8%, typical of experimental accuracy in shock tunnels. For values of  $M \sqrt{\frac{C^*}{Re_x}} > 1/5$ , the data in Fig. 10 are seen to scatter and to separate into two fairly distinct branches, corresponding to the higher and lower density test conditions. Examination of Fig. 8 shows that for the two runs at the lowest densities, the pressure was essentially constant over the entire model, analogous to that in free-molecule flow. In contrast, the pressure variation for the two higher density runs was about half of that predicted by strong interaction theory. It was noted earlier the parameter governing the vorticity interaction, the shock wave heating, and the slip effects was  $M \sqrt{\frac{C^*}{Re_x}}$  only if the pressure distribution was that given by strong interaction theory. The lack of correlation for  $M \sqrt{\frac{C^*}{Re_x}} > 1/5$  can be interpreted as a consequence of the fact that the pressure is no longer adequately described by strong interaction theory.

The pressure data, Fig. 11, qualitatively show the same behavior as the heat transfer data, except that the departures are more evident. There is

virtually no strong interaction regime under the test conditions for the present experiments. Indeed, these suggest the limit on the strong interaction regime is  $M\sqrt{\frac{C^*}{Re_x}} \leq 1/10$ .

As noted earlier, experimentally it is not feasible to distinguish between the four effects encountered in the strong interaction regime because all are essentially of the same order. It can be concluded, however, that the net result of all four effects, in the case of the cold wall, is to cause a decrease in pressure and heat transfer for values of  $M\sqrt{\frac{C^*}{Re_x}} > 1/10 - 1/5$ .

Generalization of Governing Parameters. It is evident that the separate effects of the vorticity interaction, shock wave heating, transport processes at the shock, and the slip boundary conditions cannot be examined within the framework of strong interaction theory. But it is important that the mechanism governing the observed departures from strong interaction theory be better identified to guide further theoretical developments. Considerable insight into the dominant mechanism can be obtained by generalizing the parameter governing each of the higher-order effects. It was previously observed that the data correlation in  $M\sqrt{\frac{C^*}{Re_x}}$  might cease to be valid because the strong interaction description of the pressure distribution becomes inaccurate. The generalization of the governing parameters then consists of retaining the pressure terms, as opposed to assuming  $\frac{P}{P_\infty} \sim \bar{\chi}$ . Neglecting the details of the development, it can be shown that each of the higher-order effects is governed by the following parameters.

Vorticity Interaction

$$\left(\frac{\delta}{U_\infty} \frac{\partial U}{\partial y}\right)_\delta \sim \left(\frac{1}{\bar{\chi}} \frac{P}{P_\infty}\right)^{\frac{1}{2}} \quad (38)$$

Shock Wave Heating

$$1 - \left(\frac{U_\delta}{U_\infty}\right)^2 \sim \left[\left(\frac{1}{M^2} \frac{P}{P_\infty}\right)^{\frac{1}{5}} (\bar{\chi})^2\right]^{\frac{1}{3/8}} \quad (39)$$

# Surface Slip and Shock Transport Processes

$$\omega \sim \left[ \frac{M^4 C_*}{Re_x} \frac{1}{\chi \int_0^x \frac{P}{P_\infty} d\varphi} \right]^{\frac{1}{2}} \quad (40)$$

The dominant mechanisms can now be identified by inspection. Consider the heat transfer data in Fig. 10 and the effect of substituting each of the parameters, Eqs. (38), (39), and (40), for  $M\sqrt{\frac{C_*}{Re_x}}$ . The pressure data, Fig. 12, shows that both the vorticity interaction parameter and the shock wave heating parameters, when substituted for  $M\sqrt{\frac{C_*}{Re_x}}$ , would tend to aggravate the correlation of the heat transfer data. The pressure level under the lowest density conditions is smaller than that at higher densities. Consequently, when substituting Eqs. (38) and (39) for  $M\sqrt{\frac{C_*}{Re_x}}$ , the two low density branches would tend to separate. In contrast, Eq. (40) shows that parameter varies inversely with the square-root of the pressure ratio, which would tend to bring the low-density data into agreement. Hence, an improved data correlation should be obtained in terms of  $\frac{M^3 C_H}{\chi^{\frac{1}{2}}}$  and  $\frac{1}{\chi} \frac{P}{P_\infty}$  as a function of the parameter in Eq. (40).

One can employ a semi-empirical procedure to show that a consistent data correlation can be obtained in terms of the parameter governing surface slip and the transport effects. This was done by Vidal and Wittliff,<sup>48</sup> and consists of noting in Fig. 12 that the pressure distribution for each experiment is well represented by  $\frac{P}{P_\infty} \sim \frac{1}{\chi^n}$ , where the exponent,  $n$ , varies with ambient density. The parameter in Eq. (40) can then be integrated to yield

$$\omega \sim \left[ \frac{M^4 C_* (1-n)}{\frac{P}{P_\infty}} \right]^{\frac{1}{2}} \quad (41)$$

The heat transfer and pressure data can then be correlated consistently in plots

of  $\frac{M^3 C_H}{\lambda^{\frac{3}{2}}}$  and  $\frac{1}{\lambda} \frac{P}{P_\infty}$  vs  $\omega$ . Such a correlation is of practical use in that it graphically demonstrates that the slip effects and/or transport effects dominate over the vorticity interaction and shock wave heating effects in this low-density regime. The question still remains as to the relative importance of surface slip and the transport processes at the shock wave.

Surface Slip and Shock Transport Processes. The relative magnitudes of surface slip and the effects of shock transport processes in the present experiments can be assessed by comparing the boundary conditions for each, Eqs. (10), (11), (14), and (17). The ratio of the velocity decrement at the shock wave to the slip velocity at the surface and the ratio of the enthalpy decrement at the shock wave to the enthalpy jump at the surface are approximately

$$\frac{1 - \frac{u_s}{U_\infty}}{\frac{u_1}{U_\infty}} \approx \frac{1 - \frac{H_2}{H_\infty}}{\frac{H_1}{H_\infty} - \frac{H_w}{H_\infty}} \approx \frac{\lambda_s}{\lambda_w} \frac{(\frac{\partial u}{\partial y})_s}{(\frac{\partial u}{\partial y})_w} \quad (42)$$

Noting that for low temperatures,  $\lambda \sim \frac{T^{\frac{3}{2}}}{P}$ , and that the measured surface pressure can be used in the oblique shock relations to calculate the temperature ratio across the shock wave,

$$\frac{T_s}{T_\infty} \approx \frac{2\gamma(\gamma-1)}{(\gamma+1)^2} M^2 \phi^2 - \frac{(\gamma-1)^2}{(\gamma+1)^2} + \frac{4\gamma}{(\gamma+1)^2} - \frac{2(\gamma-1)}{(\gamma+1)^2 M^2 \phi^2}$$

$$M^2 \phi^2 \approx \frac{\gamma+1}{2\gamma} \frac{P}{P_\infty}$$

it is possible to estimate the relative magnitudes of the slip effects and the shock transport effects. The ambient stream temperature in these experiments was about 60°K, and the wall temperature was about 300°K. The ratio of the mean-free-path at the shock wave to that at the surface was  $\frac{\lambda_s}{\lambda_w} = 3/4$  to  $1/8$ , depending on the ambient density level. The larger value of this ratio occurred during the higher density experiments where the departures from strong interaction

theory were small. If this is to be ascribed to the shock layer becoming fully viscous, this experiment would then correspond to the initial oscillation between the shock wave and the viscous layer. The velocity gradient at the shock wave would then be small in comparison with that at the surface, and

$$\lambda_s \left( \frac{\partial u}{\partial y} \right)_s \ll \lambda_w \left( \frac{\partial u}{\partial y} \right)_w$$

At the lower densities,  $\frac{\lambda_s}{\lambda_w} \approx 1/8$ , and if the velocity gradient at the shock is taken to be comparable to that at the wall, the effects of transport processes at the shock wave would still be an order of magnitude smaller than the effects of surface slip. Consequently, it is concluded that the effects of transport processes at the shock wave were always small in comparison with those due to surface slip in the present experiments.

This conclusion is verified by the experimental data. In the discussion of wedge flows it was noted that shock wave slip was the dominant mechanism there and that the effects of shock wave slip were first apparent for  $M \sqrt{\frac{C^*}{Re_x}} \approx 1.0$ . Examination of Figs. 10 and 11 shows that the low-density departures become important at much higher densities ( $M \sqrt{\frac{C^*}{Re_x}} \approx 1/10 - 1/5$ ) than in the wedge-flow case. Moreover, the temperature at the shock wave in the wedge-flow case is about an order of magnitude greater than in the zero-angle of attack case. For these reasons, it is concluded that the dominant mechanism causing the observed low-density departures is slip at the surface.

Effects of the Pressure Jump. The final argument to demonstrate that the observed departures from strong interaction theory stem from surface slip is to compare these departures with the pressure jump. As noted earlier, the theory of Ref. 30 is based on a perturbation method applied to strong interaction theory to

examine the first-order slip effects. The theory is applicable only for the case of an adiabatic wall, due to the approximations invoked to effect a solution. In addition, this theory treats the classical velocity and temperature jump effects but neglects the pressure jump. The pressure data are compared with the theory<sup>30</sup> in Fig. 11. The pressure jump as given earlier (Eq. 24) and as given in Ref. 29 has been applied to the results of the slip analysis as follows,

$$\frac{1}{\bar{\chi}} \frac{P_w}{P_\infty} = \left[ \frac{1}{\bar{\chi}} \frac{P}{P_\infty} \right] \left[ \frac{P_w}{P} \right] \quad (43)$$

where the first term on the right is the result given in Ref. 30 and reproduced here as Eq. 29, and the second term is the pressure jump. It can be seen that the changes in the induced pressure due to alterations in the boundary layer displacement thickness are small compared with the pressure jump. The approximate theory including the pressure jump predicts the general behavior of the data, though of course the data do not correlate in terms of  $M\sqrt{\frac{C^*}{Re_x}}$  alone. It is informative to note that the approximate calculation shows that there should be significant slip effects (10% or greater) in the weak interaction regime  $M\sqrt{\frac{C^*}{Re_x}} \approx 10^{-2}$  and that the data obtained at the highest densities are close to the weak interaction limit.

Discussion of the Slip Boundary Conditions. The slip boundary conditions, given by Eqs. 14 and 17 are usually replaced by the first-order boundary conditions; that is, the mean-free-path is evaluated at the wall conditions instead of conditions at the base of the boundary layer. The validity of this approximation can be tested by transforming the correct boundary conditions, and comparing them with the first-order boundary condition. With the following transformation,

$$\bar{\Phi} = \frac{u}{U_\infty}, \quad \bar{\Theta} = \frac{H - H_w}{H_\infty - H_w}, \quad \eta = \sqrt{\frac{Re_1}{\bar{\epsilon}}} \int_0^{\bar{\eta}} \frac{1}{L} \bar{p}_0 d\bar{y}, \quad \bar{\epsilon} = \int_0^L \frac{C^* P}{L P_\infty} dx$$



the slip boundary conditions are

$$\Phi_{\eta}(0) = \frac{b_u}{2} \sqrt{\pi \gamma (\gamma - 1)} \sqrt{\frac{T_w}{T_o}} \sqrt{\frac{T_i}{T_w}} M \sqrt{\frac{C^*}{Re_L}} \sqrt{\frac{M^2 C^*}{\mathcal{F}}} \Phi_{\eta\eta}(0) \quad (44)$$

$$\Theta(0) = \frac{b_e}{2} \sqrt{\pi \gamma (\gamma - 1)} \sqrt{\frac{T_w}{T_o}} \sqrt{\frac{T_i}{T_w}} M \sqrt{\frac{C^*}{Re_L}} \sqrt{\frac{M^2 C^*}{\mathcal{F}}} \Theta_{\eta}(0) \quad (45)$$

The first-order slip boundary conditions obtain if one replaces  $\frac{T_i}{T_w}$  with unity.

If, however, the slip boundary conditions are again substituted, quadratic expressions in  $\Phi_{\eta}(0)$  and  $\Theta(0)$  are obtained. For the purpose of illustration, let us assume local similarity so that  $\Phi_{\eta}(0) = \Theta(0)$ . The resulting slip boundary condition is

$$\Phi_{\eta}(0) = \Theta(0) = \frac{\Gamma^2 \left(1 - \frac{T_w}{T_o}\right)}{2 \left(1 + \Gamma^2\right)} + \sqrt{\left(\frac{\Gamma^2}{2}\right)^2 \left(1 - \frac{T_w}{T_o}\right)^2 + \frac{\Gamma^2}{1 + \Gamma^2} \frac{T_w}{T_o}} \quad (46)$$

where

$$\Gamma = \frac{b}{2} \sqrt{\pi \gamma (\gamma - 1)} \sqrt{\frac{M^2 C^*}{\mathcal{F}}} M \sqrt{\frac{C^*}{Re_*}} \Phi_{\eta\eta}(0)$$

The first-order slip boundary condition is usually obtained by noting that all of the terms in Eq. (46) are of higher order in  $\Gamma$  than the last term under the radical so that

$$\Phi_{\eta}(0) \approx \frac{\Gamma}{\sqrt{1 + \Gamma^2}} \sqrt{\frac{T_w}{T_o}} \approx \Gamma \sqrt{\frac{T_w}{T_o}} \quad (47)$$

Examination of Eq. (46) in light of the cited experimental data shows that this boundary condition is valid only for the case of an adiabatic wall,  $\frac{T_w}{T_o} \rightarrow 1.0$ . This can be seen by invoking the strong interaction pressure distribution to evaluate the transformed chordwise variable.

For

$$\frac{P_1}{P_2} = \frac{\sqrt{3}}{2} \gamma \epsilon \left( 0.664 + 1.73 \frac{T_w}{T_0} \right) \bar{\chi},$$

$$\frac{\bar{\chi}}{M^2 C_x} = \epsilon \sqrt{3} \left( 0.664 + 1.73 \frac{T_w}{T_0} \right) M \sqrt{\frac{C_x}{Re_x}} \quad (48)$$

$$\Gamma = \frac{b}{2} \Phi_{\eta\eta}(0) \sqrt{\frac{\pi(\gamma+1)}{\sqrt{3} \left( 0.664 + 1.73 \frac{T_w}{T_0} \right)}} \left( M \sqrt{\frac{C_x}{Re_x}} \right)^{\frac{1}{2}}$$

Now, for a typical cold-wall case  $\frac{T_w}{T_0} \approx 0.1$ ,  $\Gamma \approx \frac{1}{2} \left( M \sqrt{\frac{C_x}{Re_x}} \right)^{\frac{1}{2}}$ .

The experimental data show that the low-density departures from strong interaction theory begin at  $\Gamma^2 \approx 0.1$ , and all of the terms in the correct slip boundary condition, Eq. (46), are of the same order. Consequently it is not valid to consider a first-order slip boundary condition on the basis of ordering the parameter  $\Gamma$  alone. The wall temperature effect can be of equal importance and the entire slip boundary condition must be retained for the case of a cold wall.

Comparison with Continuum Leading-Edge Solutions. In the discussion on the available theories it was noted that the leading-edge problem had been treated by Oguchi with continuum concepts assuming slip at the surface could be neglected,<sup>31</sup> and taking account of the classical (first-order) velocity and temperature jumps at the surface.<sup>32</sup> The basis for this theory was originally noted in Ref. 14 where it was shown that at the leading edge, the flow should approach a wedge flow; that is, a straight shock wave. This model is treated in detail in Refs. 31 and 32 to effect a solution. Note that in those developments the model used is one in which the shock layer is fully viscous. However, in order to use the uniform-flow Rankine-Hugoniot relations, it is required that the shear vanish at the shock wave. This is conceptually difficult to accept but the neglect of shock wave slip does not appear critical in view of the preceding discussion. In addition, the pressure jump is

neglected.

The slip and no-slip solutions, as numerically reported in Ref. 32, are compared with the present experiments in Figs. 13 and 14 as  $C_H$  and  $\frac{1}{M^2} \frac{P}{P_\infty}$  vs.  $M \sqrt{\frac{C_x}{Re_x}}$ . Both figures show again that a universal data correlation is not obtained within these parameters. In addition, both theories given by Oguchi overestimate the heat transfer. This could stem from the first-order boundary conditions which underestimate the magnitude of the slip velocity and enthalpy jump by a factor of 2 to 3.

An interesting item to be noted in the theory of Ref. 32 is the fact that a significant slip effect on heat transfer is predicted. This is in contrast to other results for zero-pressure gradient<sup>28</sup> and for a strong interaction pressure gradient<sup>30</sup> where it is concluded that there is no effect of slip on heat transfer because of the additional sliding friction term. The fact that the experiments show a decreased heat transfer level lends partial support to the solutions based on a wedge flow.

The pressure data, Fig. 14, show the same general features as the heat transfer data. The slip and no-slip solutions from Ref. 32 appear to agree with the general trend of the data obtained at the higher densities, but this is largely fortuitous because the governing parameters do not produce a general correlation. The pressure jump given by Eq. (24) has been applied to the slip solution, and it can be seen that the results are in reasonable agreement with the data obtained at the lowest test densities. Again, this cannot be interpreted as a confirmation of the theory because the theory does not produce a general correlation.

Comparison with Kinetic Theory. Solutions have been obtained by Charwat, using approximate kinetic theory, for the leading-edge problem.<sup>33, 34, 35</sup> The

pressure data reported here are not rigorously applicable for testing this theory since the measurements were made 5-100 ambient mean-free-paths from the leading edge. They do, however, provide a qualitative check on the theoretical trends. The heat transfer data obtained with the small-scale model provide detailed information throughout the transition range and offer a quantitative check on the theory.

The leading-edge heat transfer data are presented in Fig. 15, normalized by the theoretical result for free-molecule heat transfer (unit accommodation coefficient) and plotted in terms of distance from the leading edge in ambient mean-free-path length. There are two items to be noted in these data. First, both sets of data indicate that in the limit of  $\frac{x}{\lambda_m} \rightarrow 0$ , the thermal accommodation coefficient will approach unity.\* Second, the heat transfer approaches a near-constant value several mean-free-paths from the leading edge.

One point of potential importance in interpreting the heat transfer data, Fig. 15, is the fact that the model was heated by the current in the thin-film thermometers. Since the gages were not uniformly spaced, the model had a nonuniform axial temperature distribution. The model temperature was inferred after the experiments by recording the gage resistance under typical pre-test conditions. These steady-state surface temperatures are presented in Fig. 16. It can be seen that the temperature gradient near the leading edge was quite severe and one might have to

---

\* In this connection, it should be noted that the surface was titanium dioxide and no unusual attempts were made to clean the surface. In the normal course of the experiments, the model was maintained at a temperature of about 150-250°F and at a pressure of about 0.1 - 1.0  $\mu$ Hg for one to two hours before the experiment.

take account of thermal creep\* in applying these data. The correction due to thermal creep has not been included in any correlations presented here. It has been estimated that the maximum velocity due to thermal creep is about 5% of the free-stream velocity.

It was noted in the discussion of the theories (Section II) that the approximate kinetic theory for the leading edge problem<sup>33</sup> might be quantitatively inaccurate owing to the approximations employed in accounting for the incident and re-emitted molecules. The theory should, however, identify the governing parameters and provide a basis for correlating different experiments. The heat transfer data are correlated in terms of those parameters and compared with the kinetic theory in Fig. 17. It can be seen that the theoretical parameters correlate the data from the two experiments reasonably well with a scatter of about 8%. In the free-molecule limit, the theory overestimates the heat transfer by a factor of about 5. If the theory is forced to the correct free-molecule limit, as in Ref. 35, it is found that the theory predicts the heat transfer with reasonable accuracy for values of the abscissa of less than unity, the theoretical range of validity.

The pressure data are compared with the kinetic theory, Fig. 18, in a plot of  $\frac{P}{P_\infty}$  vs.  $\frac{\mu}{\lambda_\infty}$ . This form is used for the data correlation because is the basic variable in the kinetic theory.<sup>33</sup> It would be misleading to correlate the pressure data in a manner analogous to Fig. 17 because the pressure data are far outside the range of validity for that theory. It can be seen in Fig. 18 that the present data are reasonably self-consistent and indicate a near-constant pressure

---

\* The velocity induced by the higher energy molecules emitted from the hotter section of the wall.

for  $\frac{\kappa}{\lambda_{\infty}} \approx 10-100$ . Included in Fig. 18 are the pressure data from Ref. 36. It can be seen that those data fall some 50%-200% above the present data and indicate a continuing increase in pressure in the range  $\frac{\kappa}{\lambda_{\infty}} \approx 10-100$ . The present authors have been unable to find any apparent reason for this discrepancy between the two experiments from the available information.

## CONCLUDING REMARKS

This experimental study of low density viscous phenomena at near-free-molecule conditions has shown the utility and versatility of both the hypersonic shock tunnel and the sharp flat plate in low density research. Meaningful measurements in millisecond time intervals are feasible with the shock tunnel in this regime because it is possible to use high reservoir enthalpies, and hence obtain high momentum flux and energy flux in the test section. The sharp flat plate is a particularly useful tool because many of the competing low density phenomena are suppressed with this elementary configuration. Hence, the governing low density mechanisms can be isolated.

The experimental data presented for a sharp flat plate at large angles of attack are in good agreement with viscous shock layer theory and indicate that the small discrepancies between theory and experiment (10-15%) can be attributed to differing values of the Prandtl number in the theory and the experiments. Both theory and experiments indicate that the transport effects at the shock wave (shock wave slip) are negligibly small for  $\frac{1}{\cos \zeta} \frac{Re_x}{\gamma M^2 C_x} > 0.4$ .

In examining the applicable theories in Section II and V, two extensions have been made here. First, there is a pressure jump at the surface, analogous to the classical velocity and temperature jump at the surface. This effect, which is a consequence of conserving the normal component of momentum, is larger than the changes in induced pressure due to slip-induced alterations in the displacement thickness. Evidently this effect has not been considered in boundary layer analyses that include the slip boundary conditions. The second extension was to show that the first-order slip boundary conditions used in the boundary layer analyses are inapplicable for the case of a cold wall. In writing down the complete boundary condition, it was shown that since the wall temperature term is of the same order

as the governing parameter, the terms usually neglected are the same magnitude as the first-order term. Hence for  $\frac{T_w}{T_o} \approx 0.1$ , the first-order slip boundary condition is a factor of 2 to 3 smaller than the complete boundary condition.

From the results of the experiments at zero-angle of attack, it appears that slip at the surface is the dominant cause of the observed low density departures from the thin boundary layer regime. This conclusion is consistent with the observations on the pressure jump and the inapplicability of the first-order boundary conditions. The pressure jump, when applied to existing theory, brings theory and experiment into qualitative agreement. The discrepancies between experiment and theory for heat transfer might well be due to the fact that the first-order boundary conditions underestimate the velocity jump and enthalpy jump. The other low density effects are undoubtedly present; however, their combined effects are evidently small in comparison with that due to surface slip. Further studies are required to quantitatively assess the other low density effects.

The present heat transfer results define the transition to the free-molecule limit, but further experiments over a wider range of conditions and closer to the leading edge would be of value. The most pressing experimental need, however, is for high Mach number pressure data close to the leading edge. The available pressure data are not adequate to test the kinetic treatments of the leading edge problem.



#### REFERENCES

1. Shen, S. E. , "An Estimate of Viscosity Effect on Hypersonic Flow Over a Wedge." J. Math. & Phys. , Vol. 31, p. 192, 1952.
2. Shen, S. E. , "On the Boundary Layer Equations in Hypersonic Flow." J. Aero. Sci. , Vol. 19, No. 7, p. 500, July 1952.
3. Lees, L and Probstein, R. F. , "Hypersonic Viscous Flow Over a Flat Plate." Princeton Univ. Dept. of Aero. Eng. Rept. No. 195, 1952.
4. Lees, L. , "Recent Developments in Hypersonic Flow." Jet Propulsion, Vol. 27, p. 1162, November 1957.
5. Li, T. Y. and Nagamatsu, H. T. , "Shock Wave Effects on the Laminar Skin Friction of an Insulated Flat Plate at Hypersonic Speeds." J. Aero. Sci. , Vol. 20, p. 345, 1953.
6. Stewartson, K. , "On the Motion of a Flat Plate at High Speed in a Viscous Compressible Fluid - II. Steady Motion." J. Aero. Sci. , Vol. 22, pp. 303-309, 1955.
7. Kuo, Y. H. , "Viscous Flow Along a Flat Plate Moving at High Supersonic Speeds." J. Aero. Sci. , Vol. 23, p. 125, February 1956.
8. Cheng, H. K. , "Hypersonic Flow with Combined Leading-Edge Bluntness and Boundary-Layer Displacement Effect." CAL Rept. No. AF-1285-A-4, AD 243140, August 1960.
9. Cheng, H. K. , Hall, J. G. , Golian, T. C. and Hertzberg, A. , "Boundary-Layer Displacement and Leading-Edge Bluntness Effects in High-Temperature Hypersonic Flow." CAL Rept. No. AD-1052-A-9, AFOSR TN 59-1193, AD 233867, January 1960; Also IAS Paper No. 60-38, January 1960; Also J. Aero/Space Sci. , Vol. 28, No. 5, May 1961.

10. Schaaf, S. A., Hurlbut, F. C., Talbot, L. and Aroesty, J., "Viscous Interaction Experiments at Low Reynolds Numbers." ARS Jour., Vol. 29, No. 7, p. 527, 1959.
11. Bertram, M. J., "Boundary Layer Displacement Effects in Air at Mach Numbers of 6.8 and 9.6." NACA TN 4133, February 1958.
12. Hammitt, A. G. and Bogdonoff, S. M., "Hypersonic Studies of the Leading Edge Effect on the Flow Over a Flat Plate." Jet Propulsion, Vol. 26, pp. 241-246, 1956.
13. Hall, J. G. and Golian, T. C., "Shock-Tunnel Studies of Hypersonic, Flat-Plate Airflows." CAL Rept. No. AD-1052-A-10, AFOSR TR 60-142, AD 251084, December 1960.
14. Hayes, W. D. and Probstein, R. F., "Hypersonic Flow Theory." Academic Press, New York, 1959.
15. Sherman, F. S., "Transition Flow." Proceedings of Third International Symposium on Rarefied Gas Dynamics, J. Laurmann, Editor. Academic Press, 1963. Also Univ. of California Tech. Rept. HE-150-201, August 1962.
16. Young, A. D., "Modern Developments in Fluid Dynamics, High Speed Flow." pp. 375-475, Oxford, London, 1953.
17. Cheng, H. K., "The Blunt-Body Problem in Hypersonic Flow at Low Reynolds Number." Presented at the IAS 31st Annual Meeting, Paper No. 63-92, January 1963.
18. Dewey, C. F., "Use of Local Similarity Concepts in Hypersonic Viscous Interaction Problems." AIAA Jour., Vol. 1, No. 1, pp. 20-33, January 1963.
19. Mann, W. M. and Bradley, R. G., "Hypersonic Viscid-Inviscid Interaction Solutions for Perfect Gas and Equilibrium Real Air Boundary Layer Flow." Am. Astronaut. Soc., Preprint 61-19, January 1961.

20. Mann, W.M. and Bradley, R.G., "Hypersonic Viscid-Inviscid Interaction Solutions for Perfect Gas and Equilibrium Real Air Boundary Layer Flow-Extended." General Dynamics Rept. ERR-FW-160, August 1962.
21. Ferri, A. and Libby, P.A., "Note on an Interaction Between the Boundary Layer and the Inviscid Flow." J. Aero. Sci., Vol. 21, p.130, February 1954.
22. Lees, L., "Influence of the Leading-Edge Shock Wave on the Laminar Boundary Layer at Hypersonic Speeds." J. Aero. Sci., Vol. 23, pp. 594-600, June 1956.
23. Oguchi, H., "First-Order Approach to a Strong Interaction Problem in Hypersonic Flow Over an Insulated Plate." Univ. of Tokyo Rept. No. 330, June 1958.
24. Sedov, L.I., Michailova, M.P. and Chernyi, G.G., "On the Influence of Viscosity and Heat Conduction on the Gas Flow Behind a Strong Shock Wave." Vestnik Moskovskovo Universiteta, No. 3, 1953.
25. Probst, R.F. and Kemp, N., "Viscous Aerodynamics Characteristics in Hypersonic Rarefied Gas Flow." Jour. of Aero/Space Sci., Vol. 27, No. 3, p. 174, March 1960.
26. Probst, R.F. and Pan, Y.S., "Shock Structure and the Leading Edge Problem." Proceedings of the Third International Symposium on Rarefied Gas Dynamics." Edited by J. Laurmann, Academic Press, New York. To be published.
27. Kennard, E.H., "Kinetic Theory of Gases." McGraw-Hill, New York, 1938.
28. Maslen, S.H., "Second-Order Effects in Laminar Boundary Layers." AIAA Jour., Vol. 1, No. 1, pp. 33-40, January 1963.
29. Patterson, G.N., "Molecular Flow of Gases." Wiley and Sons, New York, 1956.

30. Aerosty, J., "Strong Interaction with Slip Boundary Conditions." ARL Rept. No. 64, September 1961.
31. Oguchi, H., "The Sharp Leading Edge Problem in Hypersonic Flow Rarefied Gas Dynamics." Edited by L. Talbot, Academic Press, p. 501, 1961.
32. Oguchi, H., "The Leading Edge Slip Effects in a Rarefied Hypersonic Flow." Proceedings of the Third International Symposium on Rarefied Gas Dynamics, Edited by J. Laurmann, Academic Press, New York. To be published.
33. Charwat, A. F., "Molecular Flow Study of the Hypersonic Sharp Leading Edge Interaction. Rarefied Gas Dynamics, Edited by L. Talbot, Academic Press, 1961.
34. Charwat, A. F., "Near Free Molecule Flows: Review of Analysis and Results." Rand Corporation Paper 2367, July 1961.
35. Charwat, A. F., "Theoretical Analysis of Near-Free-Molecule Hypersonic Flow at the Sharp Leading Edge of a Flat Plate." Rand Corporation Memo RM-2553-PR, May 1963.
36. Nagamatsu, H. T. and Sheer, R. E., "High Temperature Rarefied Ultra-High Mach Number Flow over a Flat Plate." Reprint 1137-GO, ARS Semi-Annual Meeting, Los Angeles, May 9-12, 1960.
37. Anon., "48-Inch Hypersonic Shock Tunnel. Description and Capabilities." CAL Rept. (no number), May 1962.
38. Hilton, J., Fabian, G. J., Golian, T. C., Wilson, M. R. and Somers, L., "Development and Performance of the CAL Six-Foot Shock Tunnel." CAL Rept. No. 120, to be published.
39. Martin, J. F., Duryea, G. R. and Stevenson, L. M., "Instrumentation for Force and Pressure Measurements in a Hypersonic Shock Tunnel." Advances in Hypervelocity Techniques. Plenum Press, New York, pp. 145-186, 1962.

40. Vidal, R. J. , "Model Instrumentation Techniques for Heat Transfer and Force Measurements in a Hypersonic Shock Tunnel." CAL Rept. No. AD-917-A-1, WADC TN 56-315, AD 97238, February 1956.
41. Hall, J. G. and Hertzberg, A. , "Recent Advances in Transient Surface Temperature Thermometry." Jet Propulsion, Vol. 28, No. 11, November 1958.
42. Vidal, R. J. , "Transient Surface Temperature Measurements." CAL Rept. No. CAL-114, March 1962; Also paper presented at the ASME Hydraulic Conference, Worcester, Massachusetts, May 21-23, 1962.
43. Schaaf, S. A. and Cyr, R. R. , "Time Constants for Vacuum Gage Systems." J. Appl. Phys. , Vol. 20, p. 860, September 1949.
44. Skinner, G. T. , "Analog Network to Convert Surface Temperature to Heat Flux." CAL Rept. No. CAL-100, AD 247277, February 1960; Also ARS Jour. , Vol. 30, No. 6, pp. 569-570, June 1960.
45. Eschenroeder, A. Q. , Boyer, D. W. and Hall, J. G. , "Exact Solutions for Nonequilibrium Expansions of Air with Coupled Chemical Reactions." CAL Rept. No. AF-1413-A-1, AFOSR 622, AD 257396, May 1961.
46. Hall, J. G. , Eschenroeder, A. Q. and Marrone, P. V. , "Inviscid Hypersonic Airflows with Coupled Nonequilibrium Processes." IAS Paper No. 62-67, paper presented at the IAS 30th Annual Meeting, New York City, 22-24 January, 1962; Also CAL Rept. No. AF-1413-A-2, AFOSR 2072, May 1962.
47. Nagamatsu, H. T. , Weil, J. A. and Sheer, R. E. , "Heat Transfer to Flat Plate in High Temperature Rarefied Ultra-High Mach Number Flow." ARS Jour. , Vol. 32, No. 4, p. 533, April 1962.
48. Vidal, R. J. and Wittliff, C. E. , "Hypersonic Low Density Studies of Blunt and Slender Bodies." Proceedings of the Third International Symposium on Rarefied Gas Dynamics. Edited by J. Laurmann, Academic Press, New York. To be published.

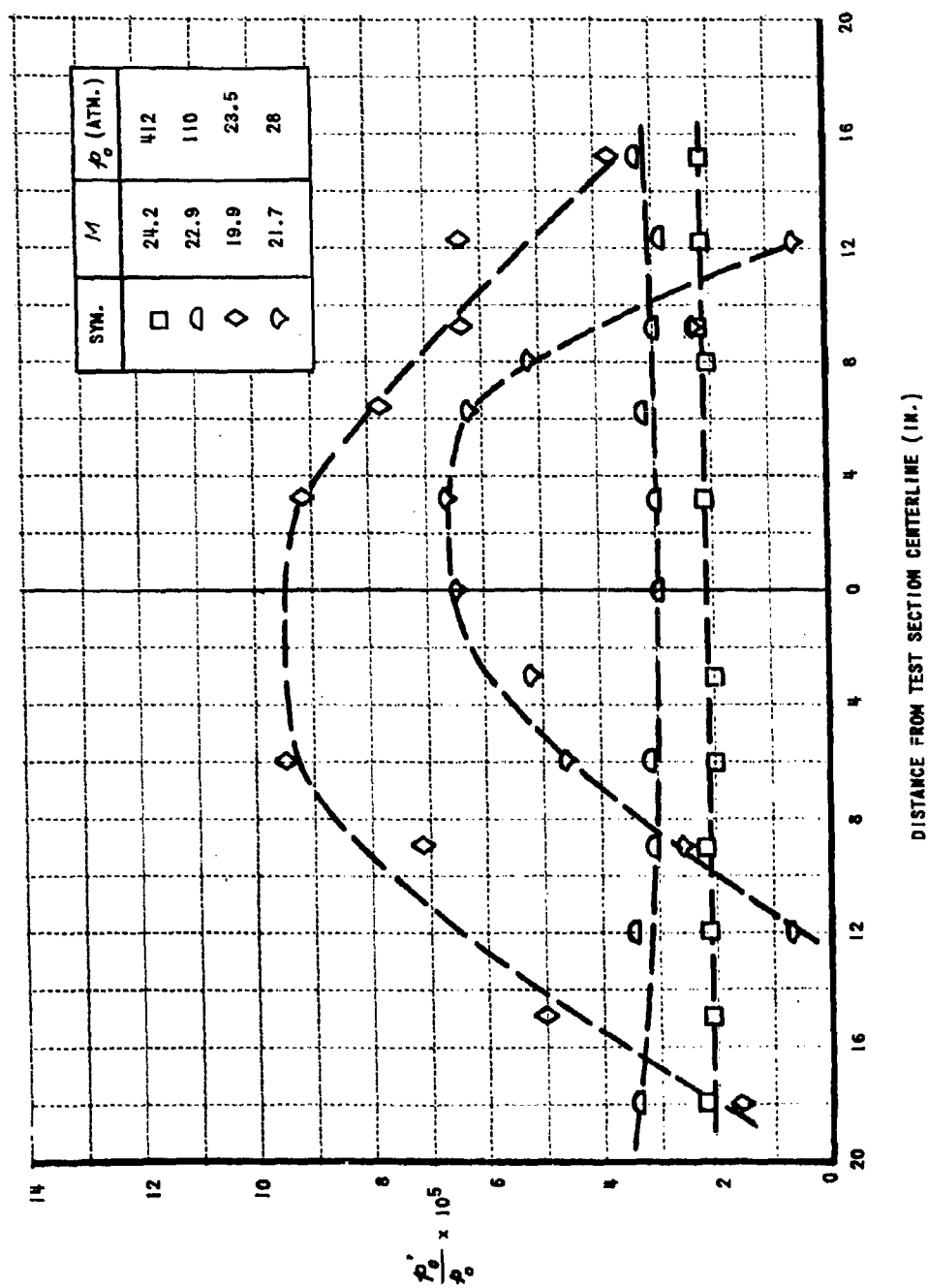


Figure 1 TEST SECTION PITOT PRESSURE DISTRIBUTION

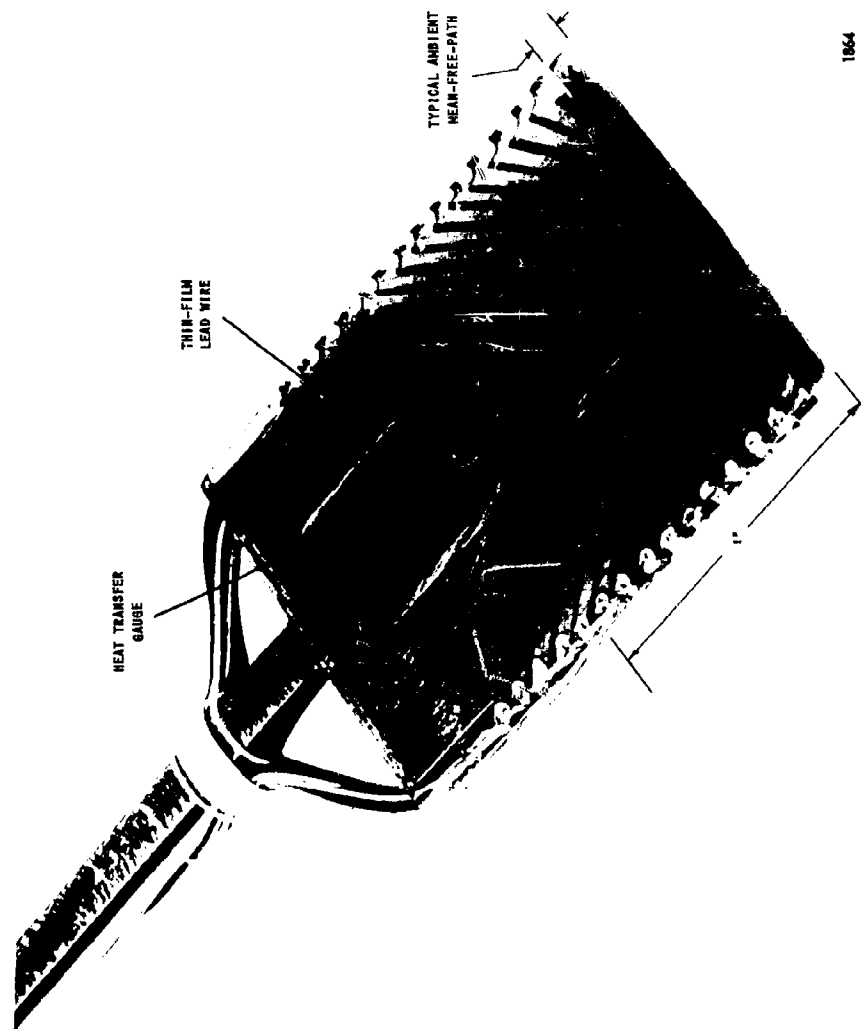


Figure 2 SMALL-SCALE FLAT PLATE MODEL

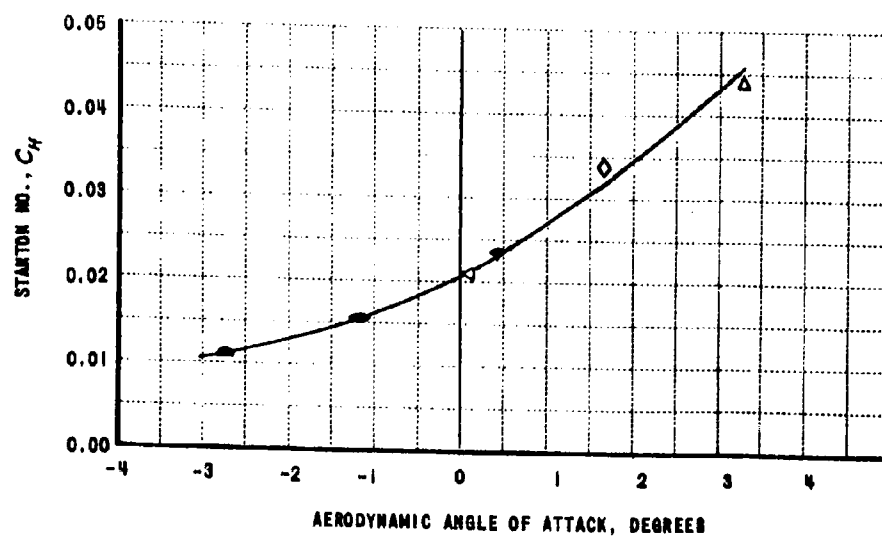
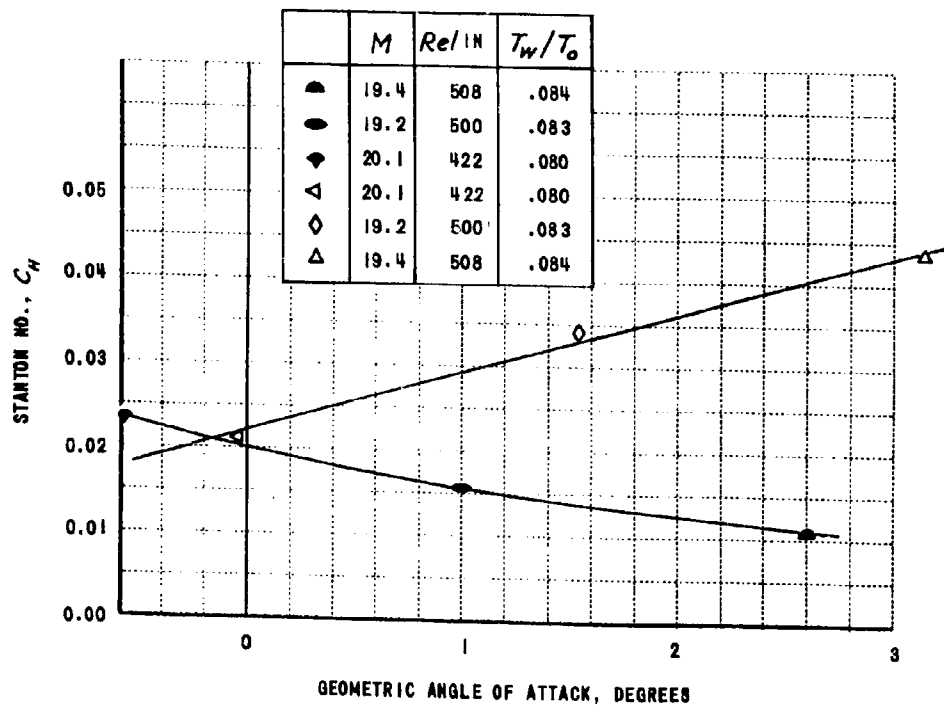


Figure 3 FLOW ANGULARITY IN THE CAL SIX FOOT SHOCK TUNNEL



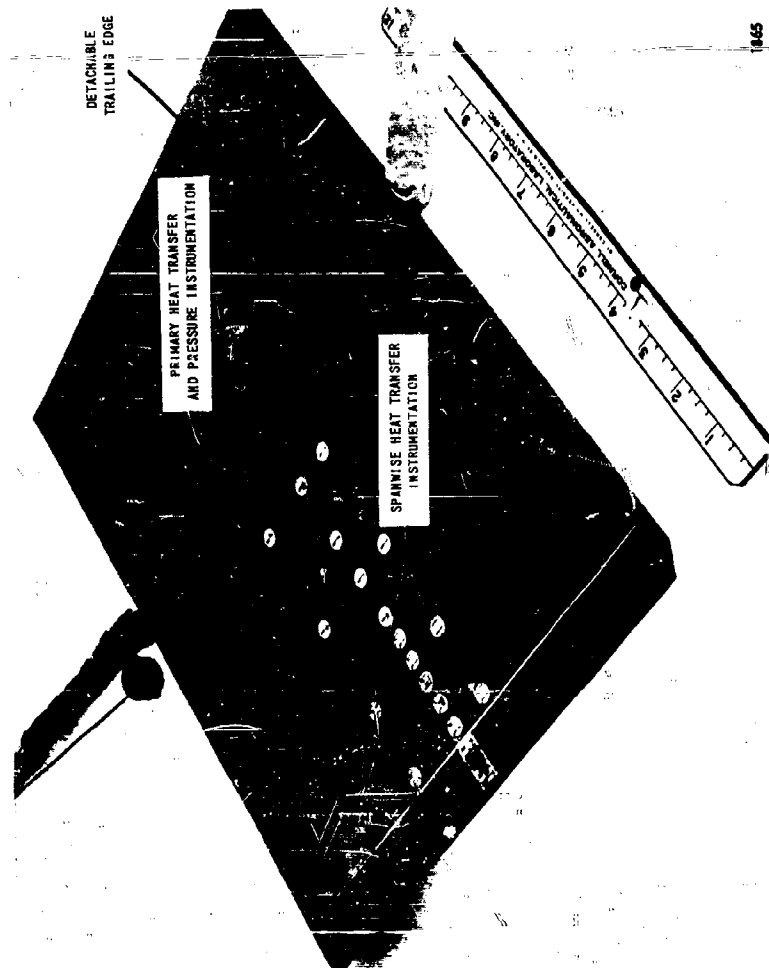
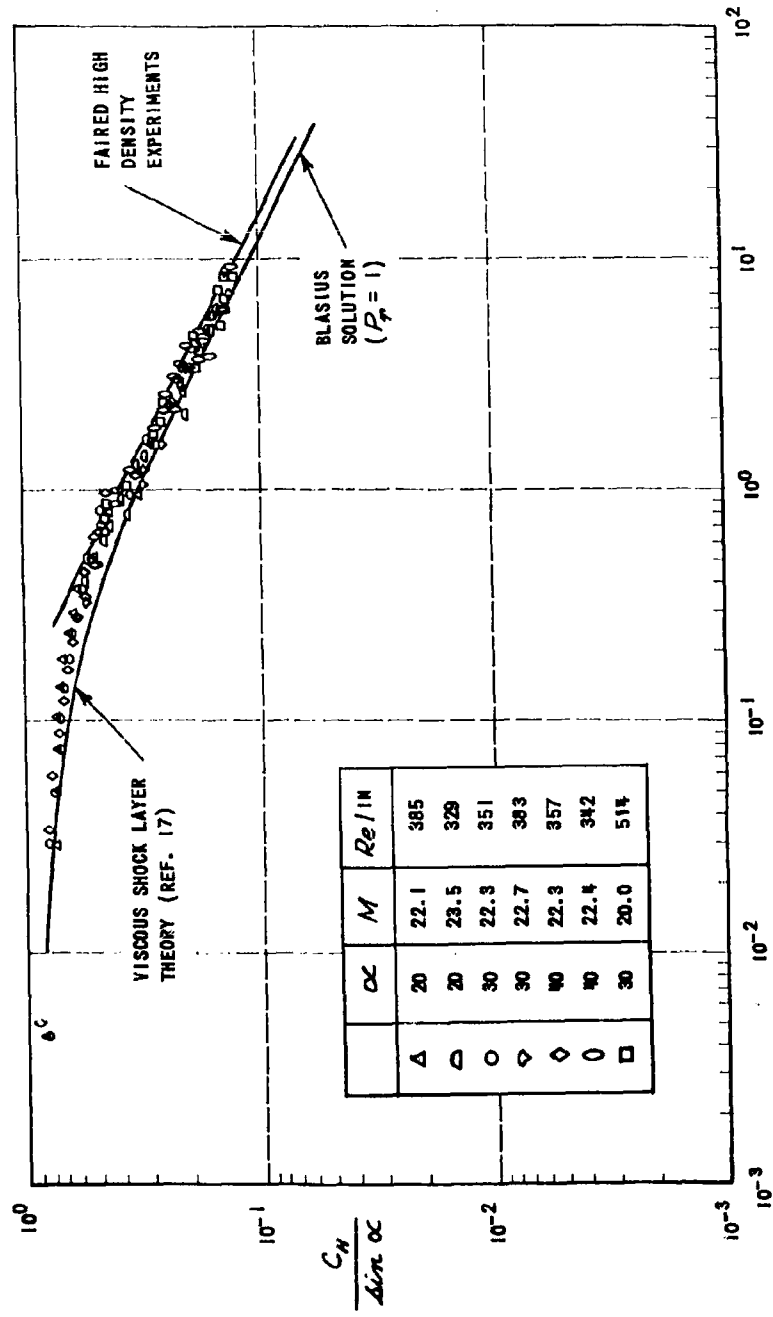


Figure 4 LARGE-SCALE FLAT PLATE MODEL



$$\frac{1}{\pi M^2} \frac{Re_x}{C_x} \frac{1}{\cos \alpha}$$

Figure 5 HEAT TRANSFER ON A SHARP WEDGE  $T_0 \approx 3600^\circ K$   $T_w/T_0 = .08$

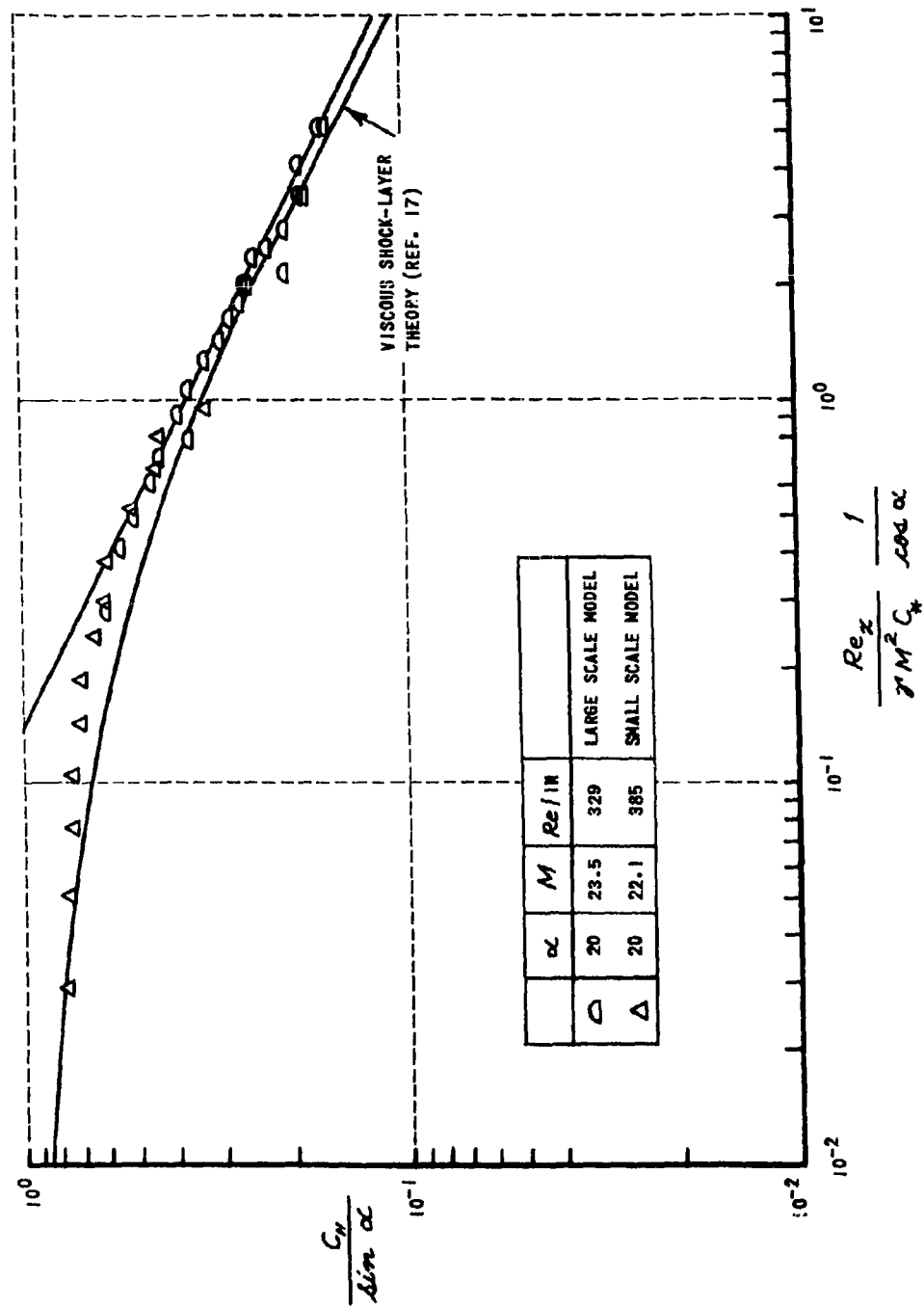


Figure 6 TRAILING EDGE EFFECTS IN WEDGE FLOW

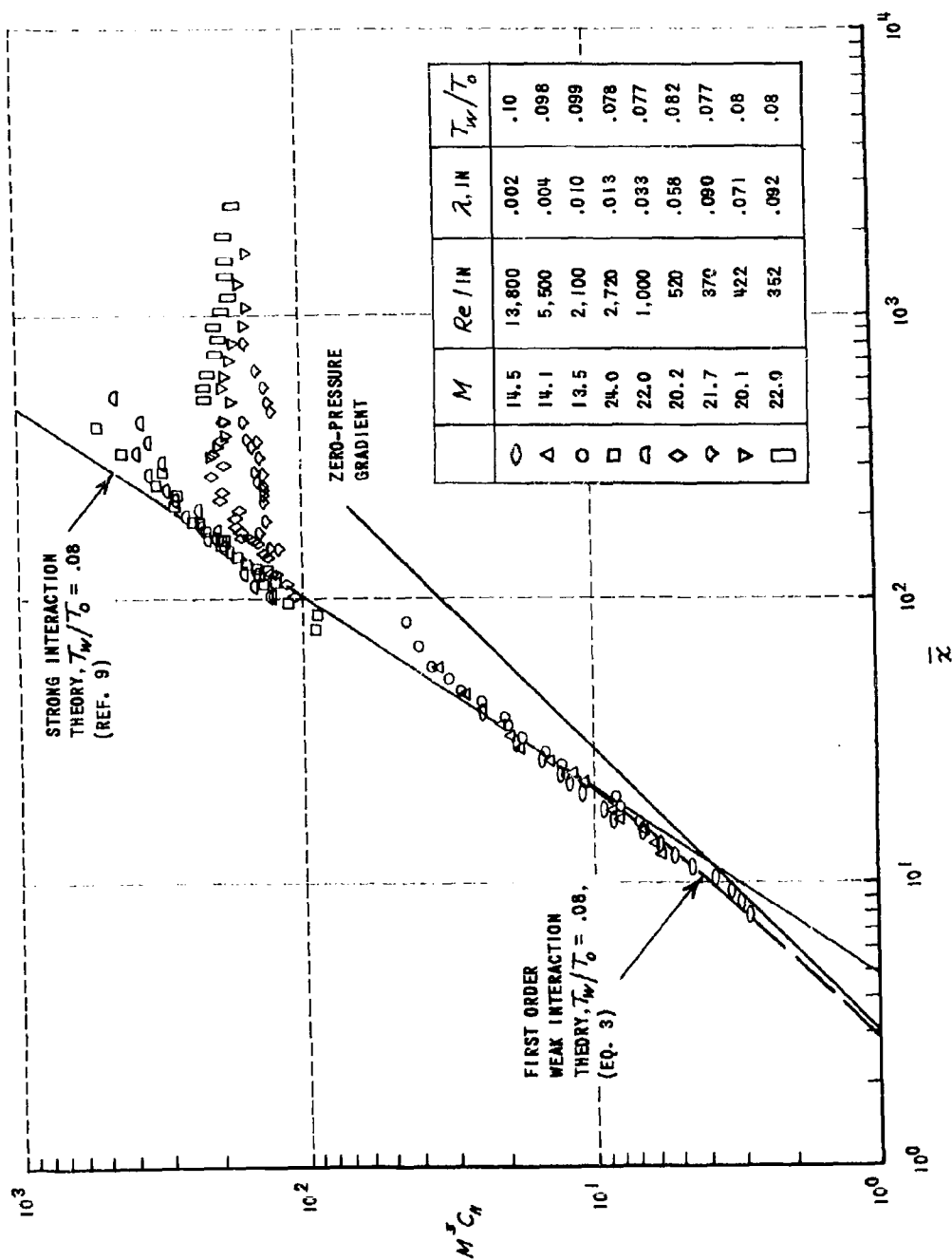


Figure 7 HEAT TRANSFER TO A SHARP FLAT PLATE

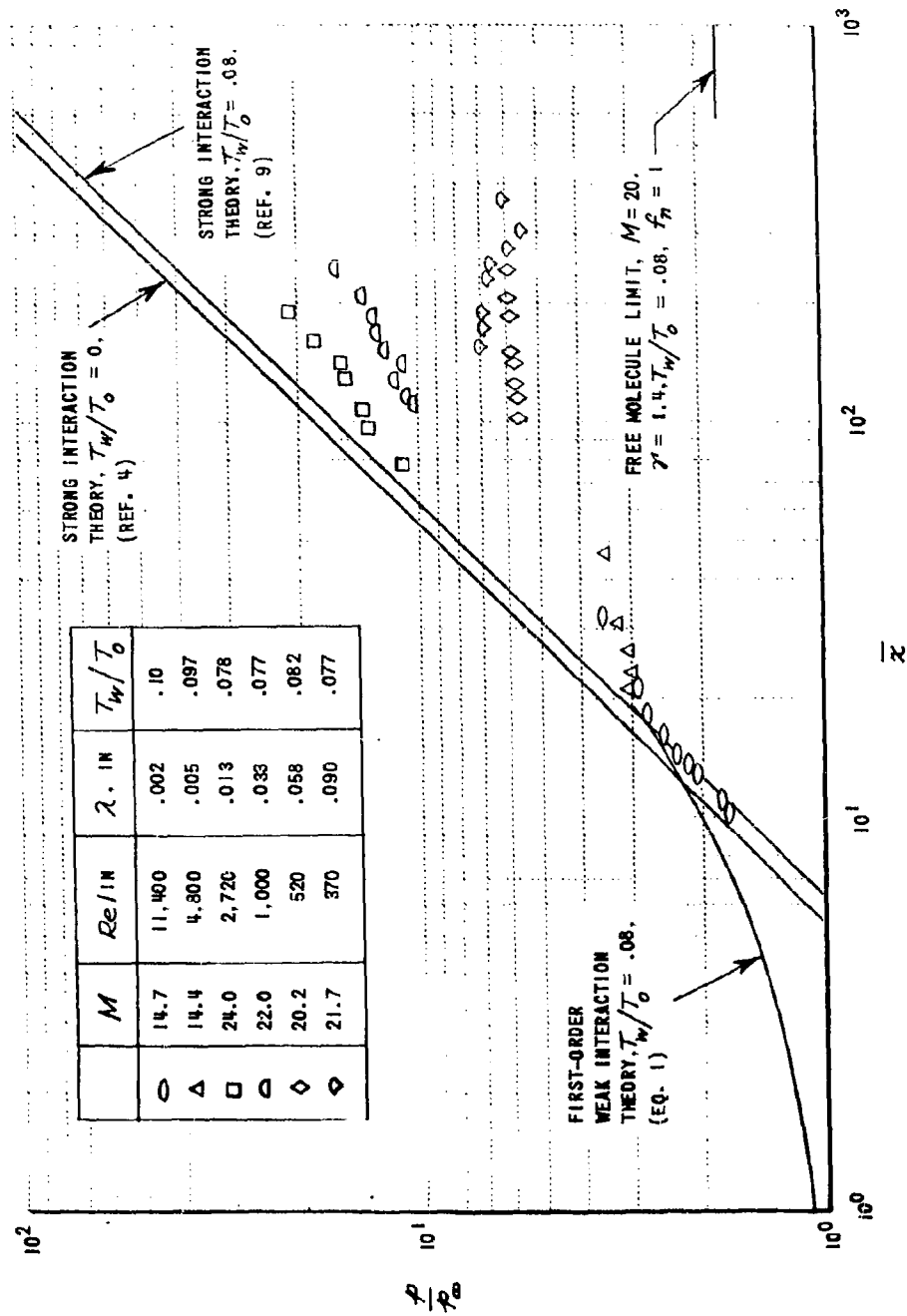


Figure 8 PRESSURE DISTRIBUTION ON A SHARP FLAT PLATE

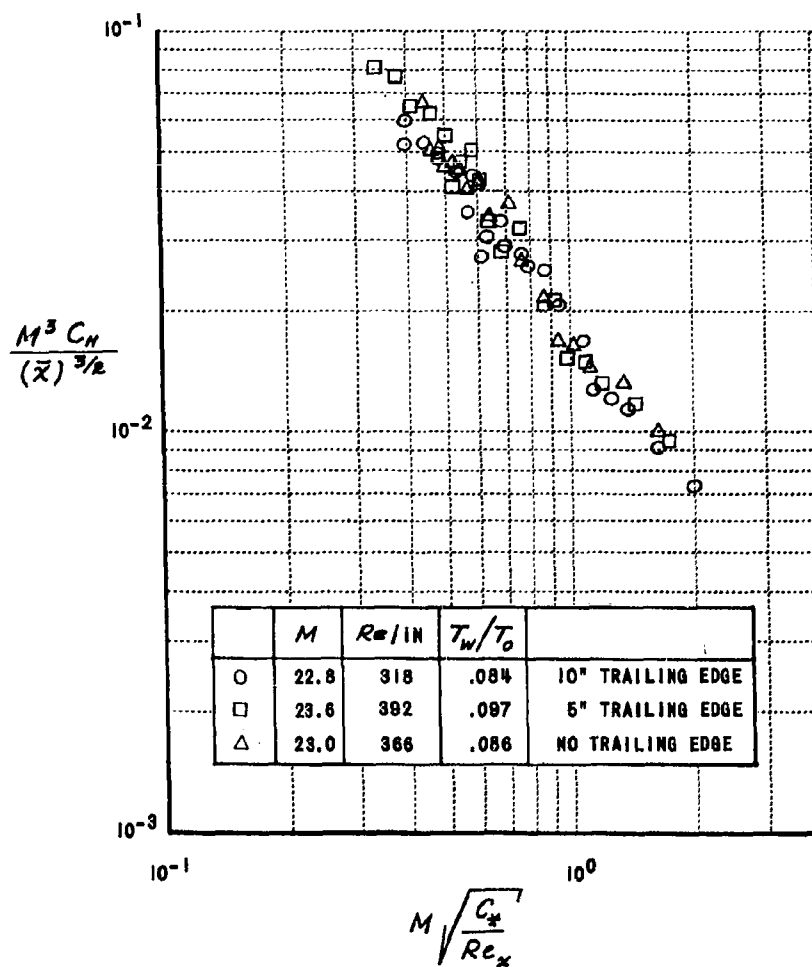


Figure 9 TRAILING EDGE EFFECTS AT ZERO ANGLE OF ATTACK

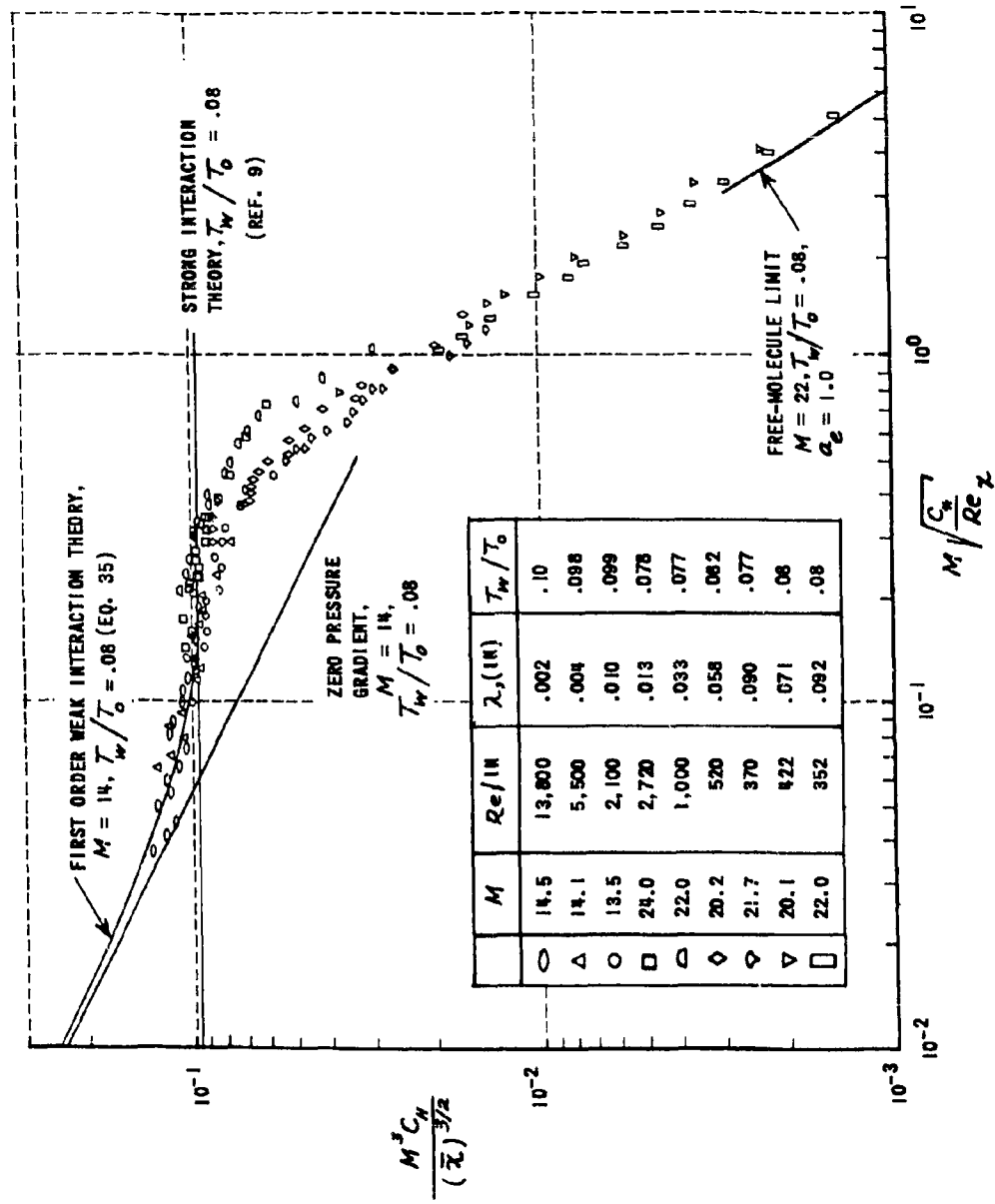


Figure 10 HEAT TRANSFER TO A SHARP FLAT PLATE

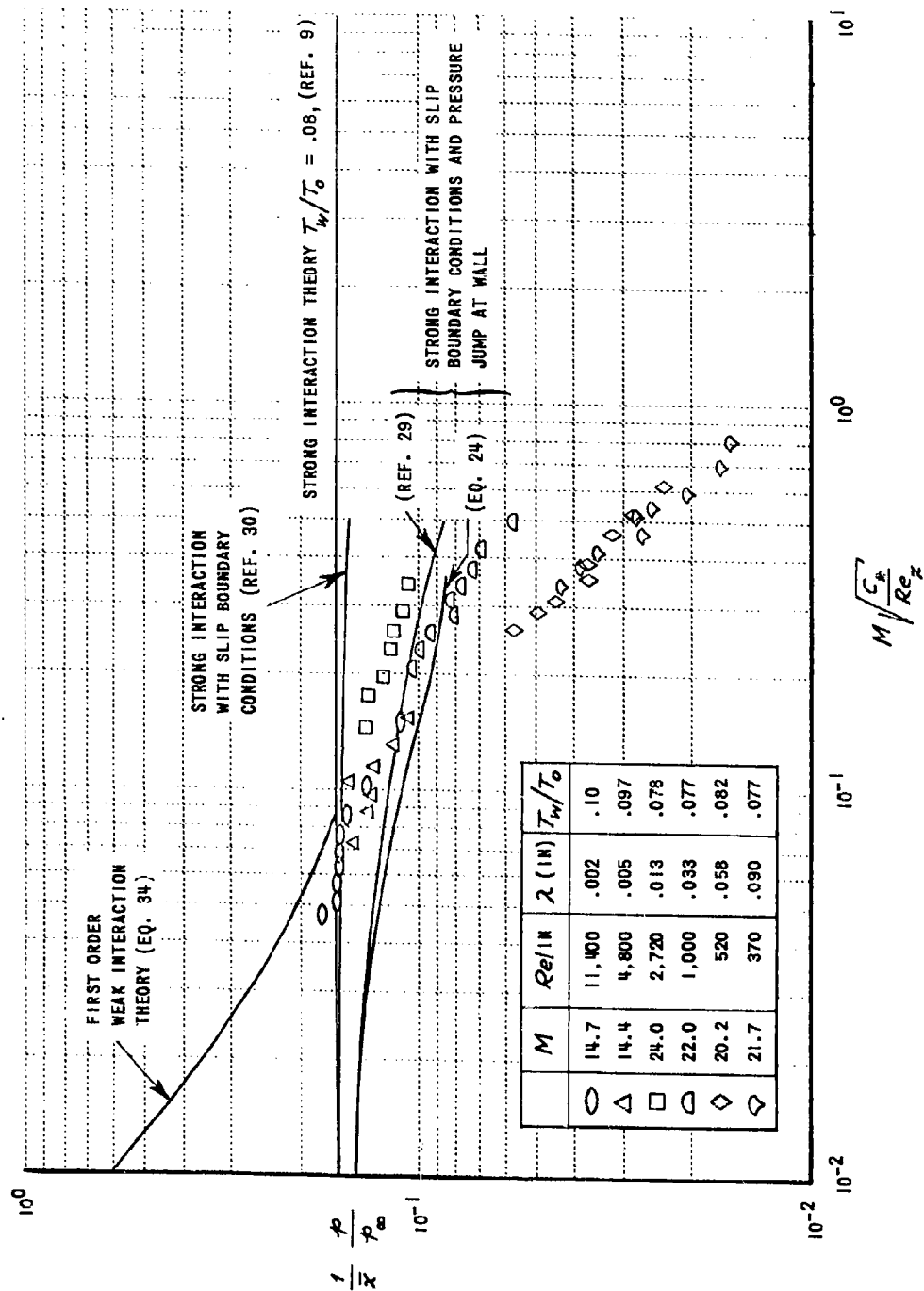


Figure 11 PRESSURE DISTRIBUTION ON A SHARP FLAT PLATE



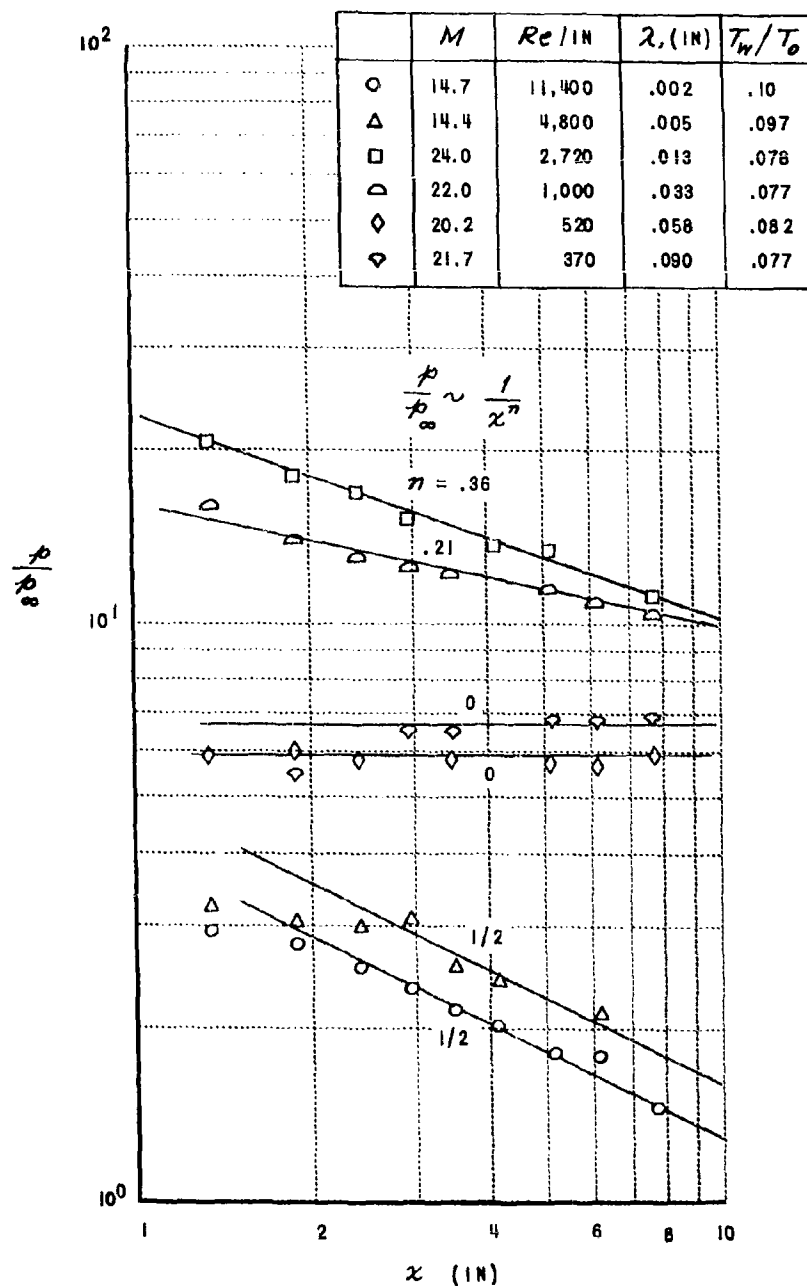


Figure 12 PRESSURE DISTRIBUTION ON A SHARP FLAT PLATE

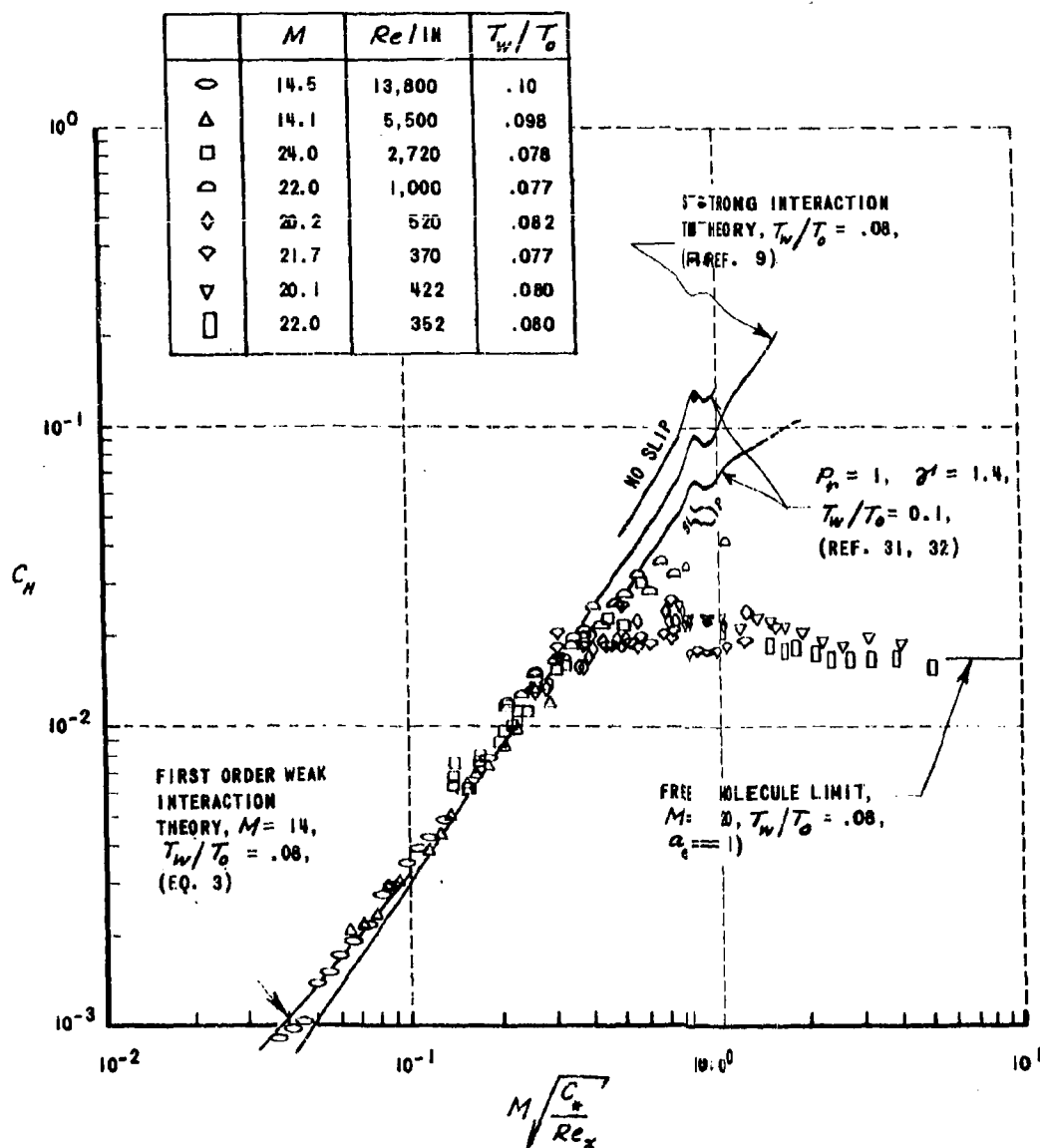


Figure 13 HEAT TRANSFER TO A SHARP FLAT PLATE

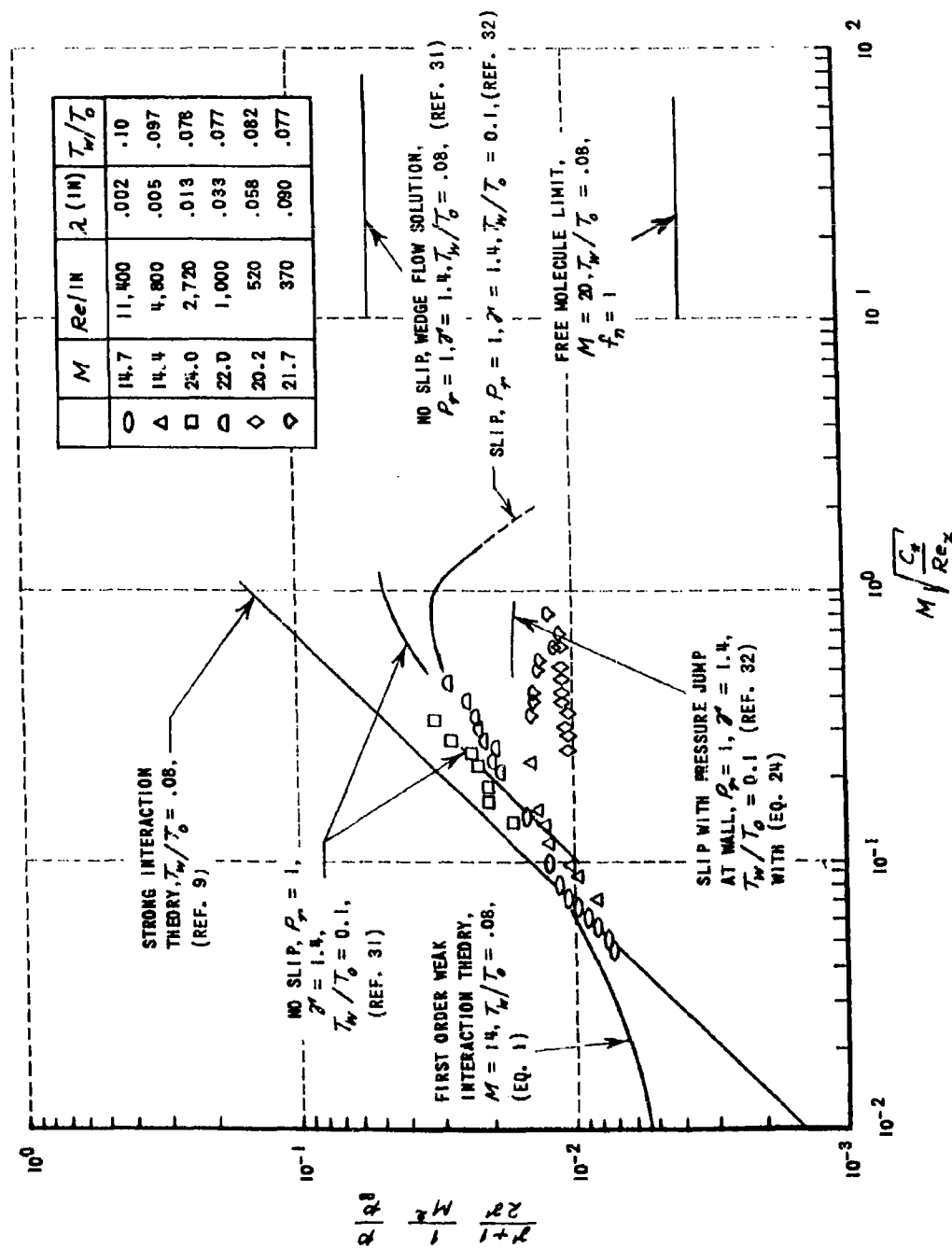


Figure 14 PRESSURE DISTRIBUTION ON A SHARP FLAT PLATE

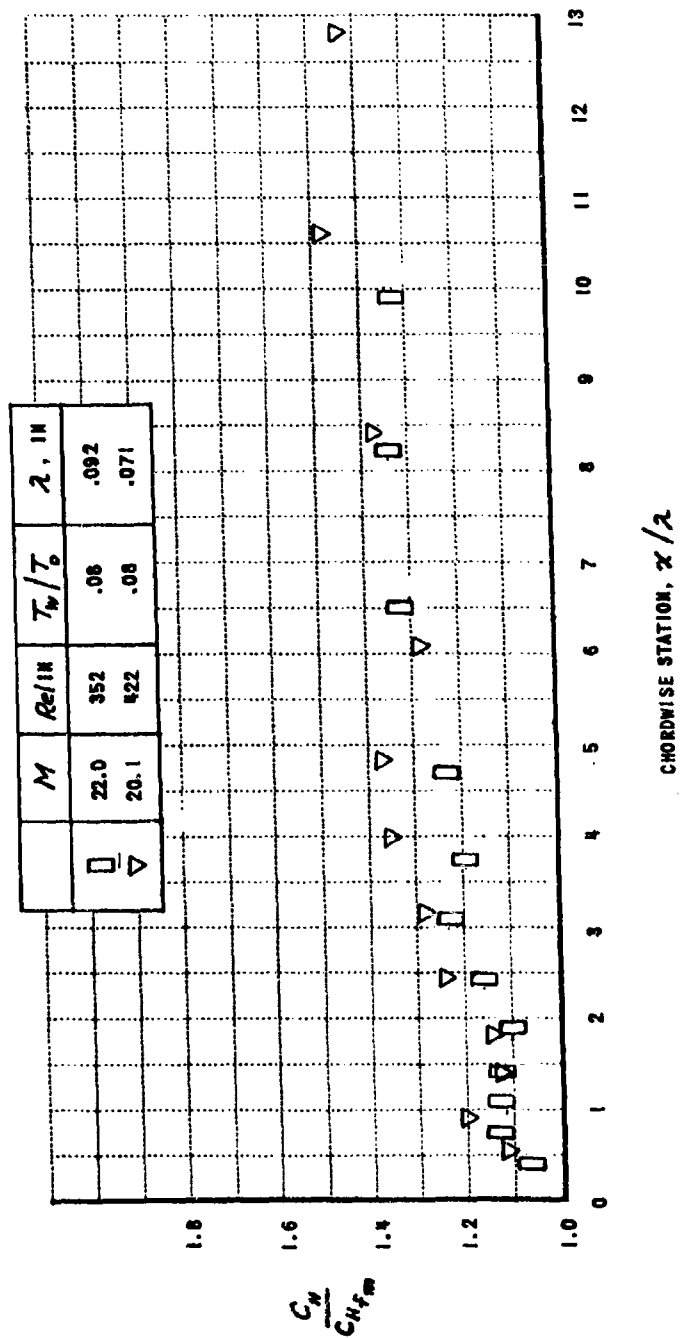


Figure 15 HEAT TRANSFER NEAR THE LEADING EDGE OF A SHARP FLAT PLATE

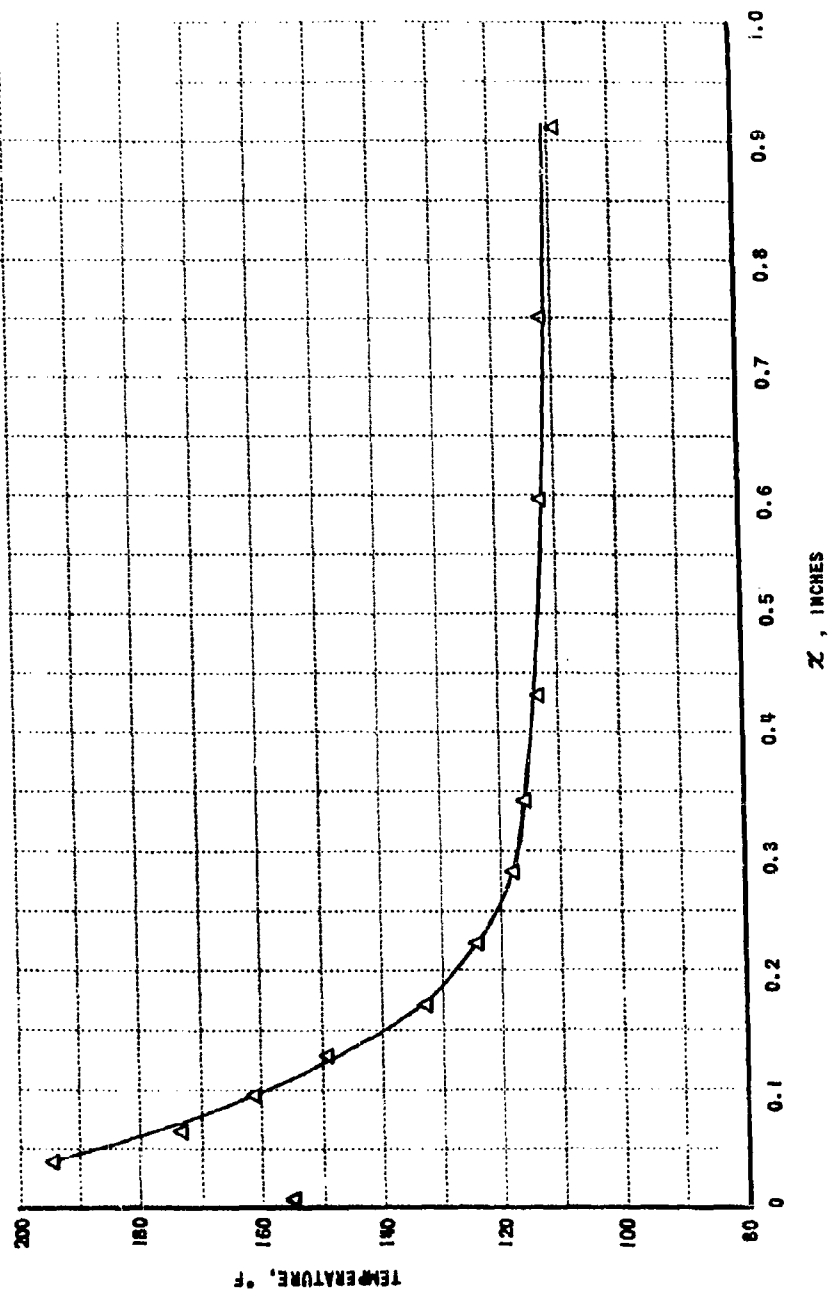
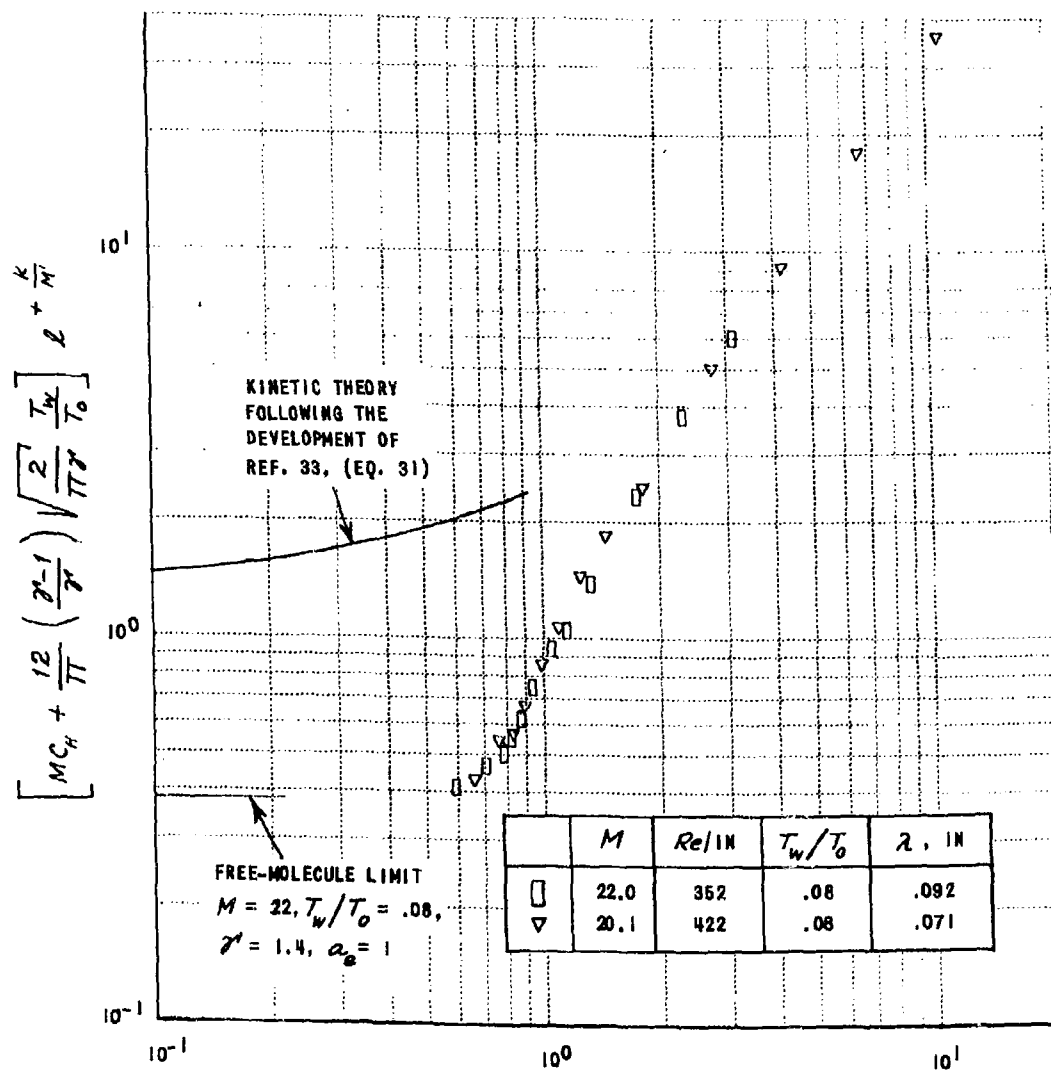


Figure 16 SHARP FLAT PLATE HEATING DUE TO GAGE CURRENT



$$\frac{M'}{K} \left( 1 - \frac{V_e}{V_n} \right)^2 \left[ -1 + \exp \left\{ -\frac{K}{M'} \left( \lambda^{-K} - 1 \right) \right\} \right]$$

Figure 17 HEAT TRANSFER NEAR THE LEADING EDGE OF A SHARP FLAT PLATE

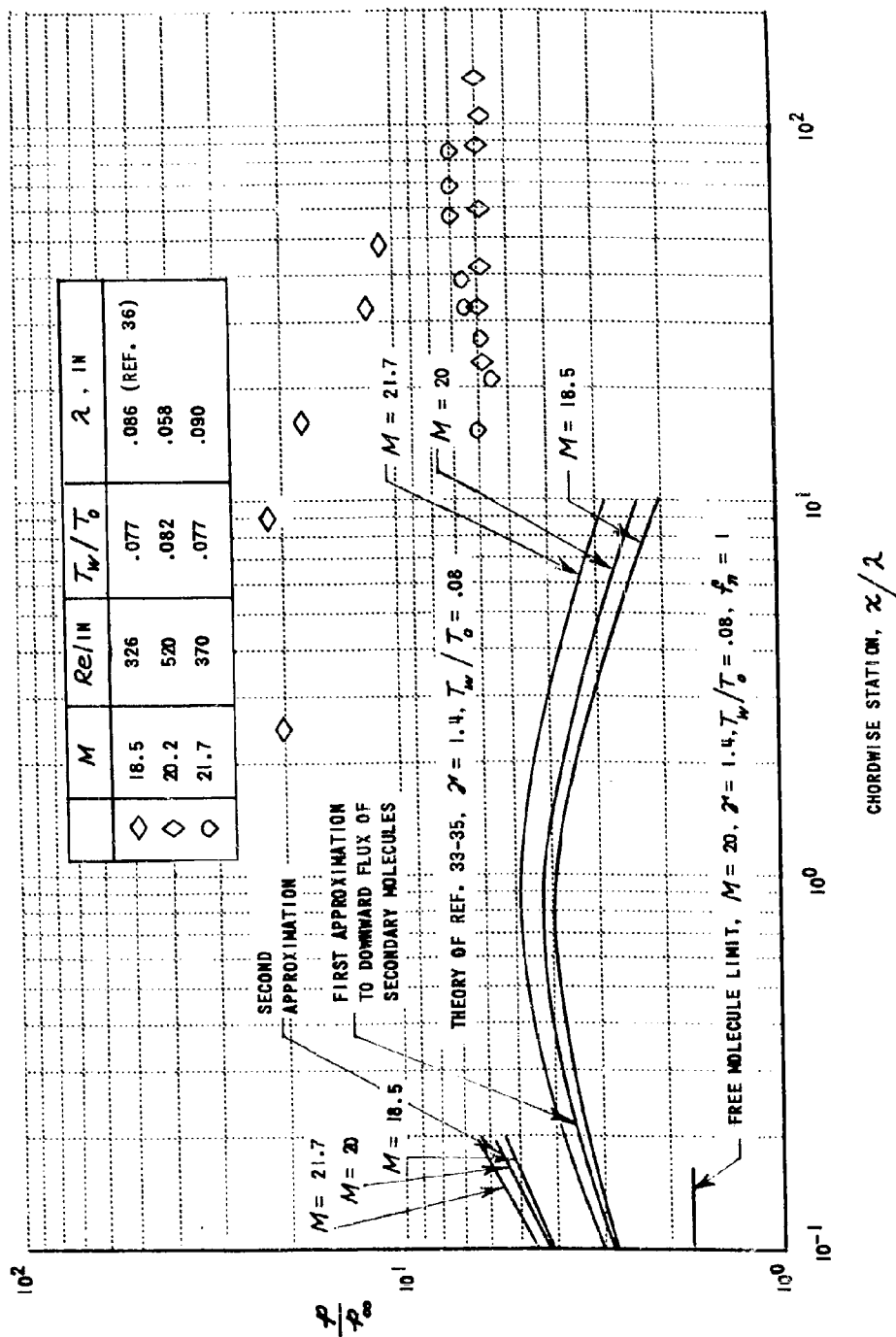


Figure 18 PRESSURE DISTRIBUTION NEAR THE LEADING EDGE OF A SHARP FLAT PLATE